Zierenberg, R.A., Fouquet, Y., Miller, D.J., and Normark, W.R. (Eds.)
Proceedings of the Ocean Drilling Program, Scientific Results Volume 169

8. Permeability, Electrical, and Thermal Properties of Sulfide, Sedimentary, and Basaltic Units from the Bent Hill Area of Middle Valley, Juan de Fuca Ridge[1]

Gerardo J. Iturrino,[2] Earl Davis,[3] Joel Johnson,[4]
Henrike Gröschel-Becker,[5] Trevor Lewis,[3] David Chapman,[6] and
Vladimir Cermak[7]

ABSTRACT

Permeability, electrical resistivity, and thermal conductivity measurements were performed on samples from the Bent Hill area of the Middle Valley on the northern Juan de Fuca Ridge. Thermal conductivity measurements were also made on samples from the Trans-Atlantic Geotraverse (TAG) hydrothermal area in the Mid-Atlantic Ridge for direct comparison with previous studies and the Middle Valley results. Electrical resistivity and permeability measurements were made as a function of confining pressure on 15 samples comprising different lithologic compositions found in the Bent Hill area. The effect of pressure on electrical resistivity values is relatively small and the observed frequency dependence is highly controlled by the sulfide content in these rocks. Permeabilities are in the 10^{-16}–10^{-20} m² (0.1–100 µD) range. Although permeability does not recover in samples that undergo significant permanent deformation, the elastic permeability dependence on confining pressure is relatively small. Permeability correlates with porosity. Permeability anisotropy correlates with the presence of oriented sulfide veins with increased flow parallel to the veins. Thermal conductivity measurements made on 41 samples from Middle Valley and 9 samples from the TAG area show systematic variations due to changes

[1]Iturrino, G.J., Davis, E., Johnson, J., Gröschel-Becker, H., Lewis, T., Chapman, D., and Cermak, V., 2000. Permeability, electrical, and thermal properties of sulfide, sedimentary, and basaltic units from the Bent Hill area of Middle Valley, Juan de Fuca Ridge. *In* Zierenberg, R.A., Fouquet, Y., Miller, D.J., and Normark, W.R. (Eds.), *Proc. ODP, Sci. Results,* 169, 1–42 [Online]. Available from World Wide Web: <http://www-odp.tamu.edu/publications/169_SR/VOLUME/CHAPTERS/SR169_08.PDF>. [Cited YYYY-MM-DD]
[2]Borehole Research Group, Lamont-Doherty Earth Observatory of Columbia University, Route 9W, Palisades NY 10964-8000, USA. **iturrino@ldeo.columbia.edu**
[3]Geological Survey of Canada, GSC Pacific - Sidney Subdivision, Pacific Geoscience Centre, PO Box 6000, 9860 West Saanich Road, Sidney, BC V8L 4B2, Canada.
[4]New England Research Inc., 76 Olcott Drive, White River Junction VT 05001, USA.
[5]Division of Marine Geology and Geophysics, Rosenstiel School of Marine and Atmospheric Sciences, University of Miami, 4600 Rickenbacker Causeway, Miami FL 33149, USA.
[6]Department of Geology and Geophysics, University of Utah, 135 South 1460 East, Salt Lake City UT 84112-0111, USA.
[7]Geophysical Institute, Czech Academy of Science, 141-31 Praha 4, Czechoslovakia.

Date of initial receipt: 3 January 1999
Date of acceptance: 14 February 2000
Date of publication: 31 August 2000
Ms 169SR-115

in composition and a weak relationship with porosity for sedimentary samples from Middle Valley. A comparison between the divided-bar and the half-space needle-probe methods of measuring thermal conductivity shows good agreement for the Leg 169 measurements unlike previous results from Legs 139 and 158. The discrepancies observed in earlier studies seem to be related to the long times used in the older measurements for the optimal T vs. ln(t) data interval. The apparatus used during Leg 169 was smaller, sampled a smaller volume of core, and in high conductivity material was not influenced by boundary effects.

INTRODUCTION

During the last three decades, the Deep Sea Drilling Project (DSDP) and the Ocean Drilling Program (ODP) have dedicated time and effort in trying to understand the geological, geophysical, and biological processes associated with spreading centers and convergent margins. Recently, significant emphasis has been placed on investigating the role that magmatic fluids and heat fluxes associated with hydrothermal systems play on the genesis of major sulfide deposits and biological communities. Circulation of hydrothermal fluids along oceanic spreading centers is one of the most fundamental processes associated with crustal accretion and localized mineralization. The styles and effects of circulation are partially controlled by the permeability and porosity of the ocean crust. Heat from magmatic intrusions drives circulation of seawater through permeable portions of the oceanic crust and upper mantle, discharging at the seafloor as both focused high-temperature (250°–400°C) flows and diffuse lower temperature (<250°C) flows. The transport of heat through this process has been estimated to comprise almost 25% of the total heat flux of the Earth (Sclater et al., 1980; Stein and Stein, 1994). This complex interaction between the circulating hydrothermal fluids and the oceanic basement greatly influences the physical properties and the composition of the crust (Thompson, 1983; Jacobson, 1992; Johnson and Semyan, 1994).

An attempt to understand the dynamic processes associated with active hydrothermal systems was made by drilling in the Middle Valley of the northern Juan de Fuca Ridge during ODP Legs 139 and 169 and the Trans-Atlantic Geotraverse (TAG) hydrothermal mound during ODP Leg 158. Most of the samples used for this study were from the Bent Hill area of Middle Valley that is located at ~48°26.2′N and 128°40.86′W. This site is in the eastern part of Middle Valley roughly 3 km west of the normal fault scarp that forms the eastern topographic boundary and ~4 km east of the current rift axis (Davis, Mottl, Fisher, et al., 1992). Hydrothermal fluids associated with the formation of the massive sulfides in this area may have been heated either locally by the intrusion of basalt underneath Bent Hill or could have been derived from a more regional, high-temperature reservoir developed by convective circulation in the upper igneous crust beneath the relatively impermeable sediment fill (Davis and Fisher, 1994). The deepest penetration in this area is 500 meters below seafloor (mbsf) in Hole 856H (Fig. **F1**). This hole consists of a 4-m layer of unconsolidated clastic sulfides overlying a 94-m massive to semimassive sulfide unit. A sulfide feeder zone consisting of sulfide veins and impregnations and a thick sedimentary unit of interbedded hemipelagic and turbiditic sediments underlie this massive sulfide unit. Below the sediments lies a 40-m-thick basaltic sill-sediment

F1. FMS log and core data, Hole 856H, p. 19.

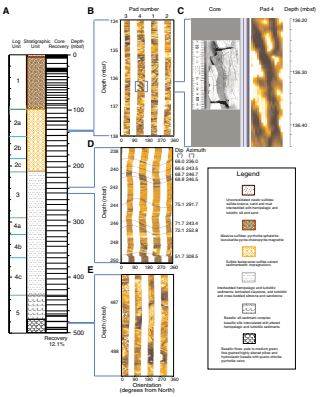

complex and basaltic flows (Davis, Mottl, Fisher, et al., 1992; Fouquet, Zierenberg, Miller, et al., 1998).

The TAG hydrothermal area, approximately located at 26°08.22′N and 44°49.55′W, is part of a 40-km-long ridge segment of the Mid-Atlantic Ridge that trends north-northeasterly. This mound is a distinctly circular feature measuring ~200 m in diameter and 50 m in height (Humphris, Herzig, Miller, et al., 1996). It is mainly a large and mature deposit composed of massive sulfide and anhydrite deposits as well as areas with active fluid flow. The observed distribution of silicified wall-rock breccias and chloritized basalt breccias recovered during Leg 158 suggests that the morphology of the mound may include several stages of evolution beginning with volcanic activity within the neovolcanic zone, subsequent spreading-related tectonic activity, brecciation, cementation, hydrothermal reworking, and, finally, sulfide and anhydrite precipitation (Humphris, Herzig, Miller, et al., 1996). A composite stratigraphic section inferred from holes drilled in three areas along a northwest-southeast transect across the mound shows four distinct zones (Fig. F2). Clast-supported massive pyrite breccias dominate the upper 10–20 m of the mound followed by an anhydrite-rich zone composed of matrix-supported, pyrite-anhydrite breccias and pyrite-anhydrite-silica breccias. With increasing depth, the amount of quartz-pyrite mineralization and quartz veining increases. This section represents the top of a quartz-sulfide stockwork zone that overlies a quartz-chlorite stockwork unit (Humphris, Herzig, Miller, et al., 1996).

Because of the low core recovery usually associated with drilling in these active hydrothermal areas (Davis, Mottl, Fisher, et al., 1992; Humphris, Herzig, Miller, et al., 1996; Fouquet, Zierenberg, Miller, et al., 1998), downhole and core physical properties measurements are extremely valuable for reconstructing complete stratigraphic sequences and, thus, an accurate series of events along their geologic history. Electrical resistivities are widely used for determining the size and extent of sulfide deposits from downhole and surface measurements. Permeability measurements are needed for assessing the extent of diffuse fluid flow associated with hydrothermal circulation. Finally, accurate thermal conductivity measurements are required for determining heat flow from temperature measurements and extrapolating thermal regimes to greater depths from near-surface temperature data.

In this manuscript, observations and interpretations are made from a limited set of measurements. We relate lithologic variations to physical parameters using thin-section observations and mineralogical estimates from visual core descriptions. All data are shown in Tables T1, T2, T3, and T4, and the methods used for the different data acquisition techniques are explained in the "Appendix," p. 15. All measurements made as a function of pressure were obtained at a constant pore pressure of 5 MPa and confining pressures ranging from 10 to 50 MPa. The 50-MPa upper limit was chosen for estimating maximum in situ conditions for boreholes drilled along Middle Valley (see "Appendix," p. 15).

PERMEABILITY

Pressure Dependence

As shown in Table T2, permeability values range from 1.6×10^{-16} to 4×10^{-20} m² (160 to 0.04 µD). The elastic permeability dependence on confining pressure is relatively minor for most samples (Fig. F3A), al-

F2. Cross section of the active TAG hydrothermal mound, p. 20.

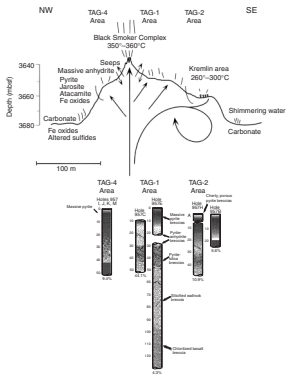

T1. Index properties and thermal conductivities, p. 34.

T2. Formation factor, resistivity, and permeability, p. 36.

T3. Comparison of thermal conductivity measurements, p. 40.

T4. Formation factor and resistivity vs. conductivity, p. 42.

F3. Permeability as a function of confining pressure, p. 21.

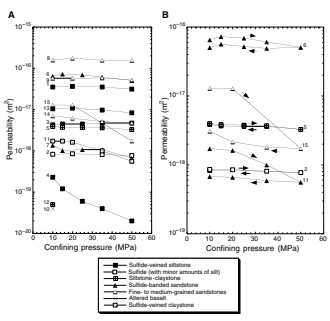

though permeability does not recover in samples that suffer significant permanent deformation. Deformation was clearly visible in some samples after testing because the ends of the cores were extruded into the core holder. This effect is evident when permeability measurements are plotted as a function of upgoing and downgoing confining pressure values (Fig. F3B). The samples that deformed the most were clay-rich samples with little or no quartz grains within the matrix.

Parameter Dependence

Permeability values at low pressures are loosely correlated with porosity (Fig. F4). A comparison between grain density and permeability measurements at low pressures shows that sandstones and several sulfide-veined siltstones tend to have higher permeabilities (Fig. F5A). Porosity values range from 4.25% to 40.2%, with sandstones having little or no sulfides and sulfide-veined samples showing higher porosity values than the sulfide-bearing minicores (Fig. F5B; Table T1). Vertical samples containing sulfide veins that are horizontally to subhorizontally oriented (or perpendicular to the long axis of the minicore) tend to have lower permeabilities than their adjacent horizontal pairs. These results suggest that there might be a significant degree of permeability anisotropy associated with oriented sulfide veins (Fig. F6). However, variations in matrix composition and the distance between samples (Table T2) may also affect these measurements.

Even though results indicate that matrix variability may affect permeability, this is not evident in four cores with minor amounts of sulfide that show permeabilities ranging from 3.9×10^{-18} to 1.58×10^{-16} m^2 (Samples 5, 8, 9, and 15 in Table T2). Although whole-rock chemical analyses were not performed, thin-section observations suggest that these cores do not have a clear relationship between clay or silt content and permeability. The only basaltic sample analyzed (Sample 169-856H-65R-2, 71–73 cm) has the lowest permeability of any sample measured (3.7×10^{-20} m^2; Table T2).

Comparison with Previous Results

Results from Leg 139 packer and laboratory experiments indicate that there are at least three hydrological types of formations in the Middle Valley hydrothermal system (Becker et al., 1994; Fisher et al., 1994). These are (1) faults with very high permeability, (2) extrusives and a sediment/sill complex with an intermediate average permeability of 10^{-14} m^2, and (3) sediments having a low average permeability on the order of 10^{-16} m^2. The results from this study show that the permeability of one basalt sample is up to six orders of magnitude less than basement permeabilities obtained from downhole measurements, whereas the sediments are up to two orders of magnitude less than laboratory measurements on shallower sediments from Sites 856, 857, and 858 along Middle Valley (Fisher et al., 1994). These results suggest that most of the basement permeability is associated with fractures or faults similar to those interpreted from seismic results (Davis and Villinger, 1992; Rohr and Schmidt, 1994). Lithologic variations and increased pressure with depth may cause the difference in the permeability of the sediments. These differences are addressed in "Discussion and Conclusions," p. 10.

The estimated in situ pressure in Hole 856H ranges from 24 MPa at seafloor to ~38 MPa at 500 mbsf (see "Appendix," p. 15). As shown in

F4. Correlation between log permeability and log porosity, p. 22.

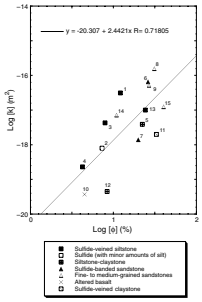

F5. Comparison between grain density and permeability, p. 23.

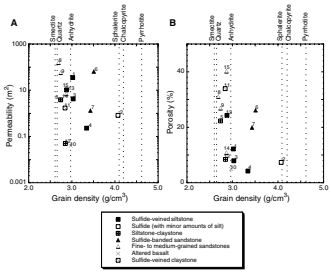

F6. Permeability anisotropy measurements, p. 24.

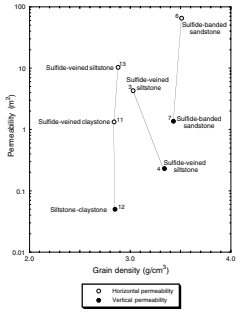

Figure F3, the low permeability and the dependence on confining pressure exhibited by several samples (i.e., Samples 4, 6, 11, and 15) suggest that the overburden pressure and consolidation within the thick sedimentary section in this area should reduce permeability significantly with depth. This may have a notable effect on the ability of hydrothermal fluids to flow through the sedimentary section in this hydrothermal system.

ELECTRICAL IMPEDANCE

Pressure Dependence

Formation factors (sample resistivity divided by fluid resistivity) were computed using the real component of the complex resistivity. Most samples show a mild increase in formation factor with confining pressure (Fig. F7). For some cores this is an elastic response, whereas other samples show nonrecoverable deformation. Results also show that, generally, formation factor increases slightly as permeability decreases, which may be due to the closure of cracks and increased grain contact within the clay-rich matrix. However, a permanent change in formation factor does not seem to correlate in every sample with a permanent change in permeability (Fig. F8). In particular, two samples (169-856H-21R-1, 78–80 cm, and 169-1035F-10R-1, 25–27 cm) display a very different behavior as a function of pressure, where formation factor decreases with decreasing permeability (Fig. F8). These results may demonstrate the effects of crack closure within a sulfide-rich matrix.

Frequency Dependence

In clay mineral–rich rock, resistivity measurements can have frequency dependence because clays tend to preferentially absorb cations. This dispersive behavior is caused by induced polarization in water-bearing materials (Wong, 1979). Clay effects are not usually observed experimentally, however (Marshall and Madden, 1959), and they were not seen in the measurements reported here.

In contrast, induced polarization is particularly pronounced in rocks containing sulfide minerals due to electrochemical effects (Wong, 1979; Klein et al., 1984). In such cases, sulfide-bearing samples appear more resistive at low frequencies than they would without any sulfides. As frequency increases, resistivity decreases asymptotically to values much lower than that of the same rock matrix with no sulfides. This effect is evident when the current is transferred from metal to ionic conduction at the sulfide/fluid interfaces, and it is induced by oxidation-reduction reactions triggered by ions in the fluid. A concentration of ions builds up and the resulting electric field retards the chemical reactions (Wong, 1979). At higher frequencies of alternating current, less of an ionic concentration develops, resulting in a lower impedance. A common explanation of this phenomenon is that diffusion of ions into and away from the interfaces causes the impedance. However, experimental studies show that different sulfide minerals conduct current with different reduction-oxidation reactions that are not strictly diffusion dependent (Klein et al., 1984). Furthermore, a theoretical model of sulfide-bearing ores (Wong, 1979) shows that frequency is a function of the size distribution of sulfide grains and that the slope of frequency dependence is a function of the percentage of sulfide material in the rock. This model

F7. Formation factor as a function of confining pressure, p. 25.

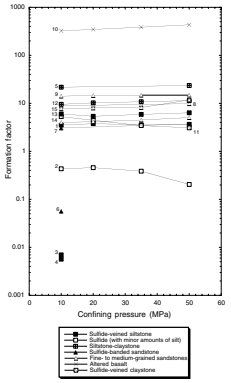

F8. Permeability and formation factor as a function of confining pressure, p. 26.

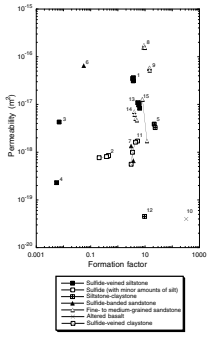

assumes spherical grains, which is not a reasonable assumption for Middle Valley cores, but it may qualitatively help to explain some of the observations.

Using the method 1 experimental configuration (see "Appendix," p. 15), 6 of 15 cores were electrically shorted due to interconnected sulfide veins running across the length of the minicore. Similar problems have been recorded with downhole resistivity measurements in massive sulfides zones (Fouquet, Zierenberg, Miller, et al., 1998). However, electrical resistivities obtained using method 2 (see "Appendix," p. 15) show a strong frequency dependence caused by the reduction-oxidation reactions occurring at the metal/fluid boundaries. Using method 2, a frequency-dependent behavior separates the sulfide-bearing minicores from the clay-rich samples containing no sulfides (Fig. F9). Formation factor decreases with increasing frequency in sulfide-bearing samples, whereas clay-rich minicores with little or no sulfides do not change with frequency. In addition, some sulfide-rich samples show stronger frequency dependence than others. Visual sample descriptions suggest that the magnitude of the frequency dependence is related to the amount of sulfides within individual samples.

Formation factor for six cores (Samples 1, 2, 11, 12, 13, and 14) changes as a function of frequency (Fig. F9). If one assumes that the matrix is similar for these samples, then at low frequencies a core with sulfide minerals will appear more resistive than its sulfide-free equivalent because of induced polarization. Based on visual and thin-section observations, the assumption of a common clay/silt matrix for most of these samples is reasonable; thus, induced polarization may be contributing to changes in formation factor.

F9. Formation factor and frequency obtained with method 2, p. 27.

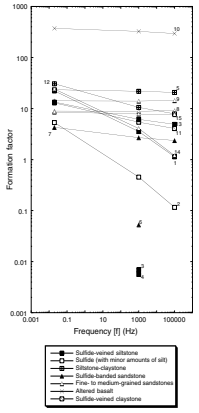

Parameter Dependence

Because of the relatively small number of samples used for the electrical resistivity measurements, it is difficult to distinguish significant trends among formation factor, porosity, density, and permeability. Frequency dependence and visual descriptions indicate that grain density values >3.00 g/cm³ correlate well with sulfide content (Fig. F10A). In addition, most of the sulfide and sulfide-bearing samples have the lowest porosity and the largest frequency dependence (Fig. F10B). No clear correlation between formation factor and permeability is observed (Fig. F8) although, in most cases where pressure reduces permeability, the formation factor increases slightly.

Differences in clay content can correlate with variations in the formation factor by a factor of two or more. Sample 169-856H-25R-3, 16–18 cm, has minor amounts of sulfide minerals and exhibits minor frequency dependence (Fig. F9). Thin-section observations show that this sample contains significant amounts of quartz and has a formation factor of 22. Sample 169-856H-44R-1, 92–94 cm, is sulfide free but contains silt-sized quartz grains and has a formation factor of 15. The most clay-rich cores (Samples 169-856H-41R-1, 29–31 cm, and 169-1035F-17R-1, 29–31 cm) have formation factors in the range of 8–10. Thin-section observations also show that these two high-porosity samples (31.1% and 40.2%) have few empty voids. In these cases, most of the apparent porosity seems to be either submicroscopic or due to the clays absorbing most of the water. Either bound or free water could be responsible for conducting a significant amount of current through the samples.

F10. Formation factor and grain density as a function of frequency, p. 28.

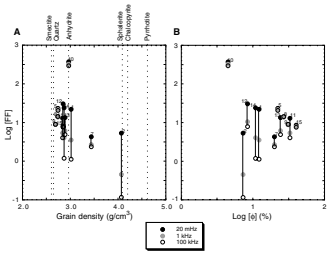

The effect of brine concentration on sample resistivity was addressed with Sample 169-856H-25R-3, 16–18 cm (Table T4). This sample has a clay- and quartz-rich matrix with small amounts of disseminated sulfides. Brine conductivity was varied between 5.1 and 16.2 mS/cm. Over the range of fluid concentrations tested, the effect on sample conductivity is roughly proportional to the fluid conductivity when plotted on a log-log scale (Fig. F11). However, because this analysis was performed in only one sample, there are several factors to consider. First, pore fluid was flushed through the sample until steady-state resistivity was reached. In this particular case, the sample required several days to equilibrate when the brine was changed. This may have been caused by clay chemistry and may be different for more quartz- or sulfide-rich samples. Also, only NaCl brine was used and different salinities may have different effects on the internal structure of the sample. Finally, the sulfides are very chemically reactive and possible changes due to temperature effects and reduction-oxidation reactions from large sulfide concentrations have not been explored.

Several samples from the sulfide feeder zone contain sulfide veins oriented both perpendicular and parallel to the long axis of the minicores as well as disseminated sulfide nodules. However, even though there seems to be a significant degree of permeability anisotropy due to preferred orientation of sulfide veins, it is still unclear whether resistivity measurements can resolve these differences in vein geometry, other than determining whether or not veins are interconnected across the sample.

F11. Relationship between sample and fluid conductivities, p. 29.

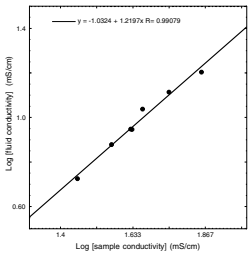

Effects of Methodology on Resistivity

The difference in measuring electrical resistivity between methods 1 and 2 depends on the sulfide content within the sample. Lithologies such as sandstones and carbonates are insensitive to the measuring technique (New England Research Laboratory, unpubl. data). However, for cores with interconnected sulfides, method 2 shows that resistivity has a strong frequency dependence instead of giving electrical shorts. Cores containing sulfides that do not interconnect show a frequency dependence that does not vary significantly with methodology.

The sensitivity to measurement method of other sulfide-bearing samples is more subtle, as in the case of Sample 169-1035F-12R-1, 132–134 cm. This minicore contains sulfides that are not interconnected across the sample and do not give an electrical short using method 1. Results show that even though there is frequency dependence using both methods, there is a smaller decrease in resistivity and less frequency dependence when using method 1 (Fig. F12A). Formation factor is somewhat lower using method 1 (Table T2) because, without the polyester screens, the voltage electrodes seem to touch several sulfide minerals at the end of the cores and direct some of the applied current to flow directly into the electrodes. Presumably, this also explains the fact that frequency dependence is somewhat lower when using method 1.

In contrast, Sample 169-856H-21R-1, 78–80 cm, is almost completely composed of conductive sulfide minerals. Using method 2, resistivity shows strong frequency dependence (Fig. F12B). Using this method the sample resistance varies from 198 W at 20 mHz to 5.8 W at 100 kHz, whereas method 1 gives a dead electrical short at ~0.1 W over the same range of frequencies (Fig. F12C). Using the method 2 resistance for this sample at 20 mHz, a direct measure of the chemical reaction impedance at the 2.54 cm sulfide/brine interface may be inferred. To determine the

F12. Resistivity measurements using methods 1 and 2, p. 30.

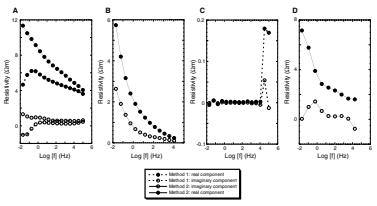

resistance associated with the electrodes, resistivity was measured with no rock sample and only the polyester screens between the electrodes (Fig. F12D). The voltage electrodes have measurable impedance because reduction-oxidation reactions also take place between the brine and the voltage electrodes. Even though the electrodes have a capacitance, the measured electrode resistance at 20 mHz is in the range of 7 W. The remainder of the impedance is assumed to be from the sulfide/brine interface.

A significant observation from Figure F7 is that the sulfide-bearing samples do not necessarily appear different from the cores without sulfides when resistivity is measured at a single frequency. These results seem to suggest that the imaginary component of complex resistivity can be used to discern the presence of sulfide minerals. However, determination of sulfide content using geochemical analyses and more measurements will be needed in the future to assess the validity of this method. Whether or not this technique can be applied to downhole measurements is not clear at this time.

THERMAL CONDUCTIVITY

Parameter Dependence

Thermal conductivity measurements were performed on 41 samples from Middle Valley and 9 samples from the TAG hydrothermal area (Table T1). A subset of these thermal conductivity measurements (Table T3) was compared with previously published data collected with the same method (Gröschel-Becker et al., 1994; Rona et al., 1998). The results show some systematic variations due to changes in composition but no clear relationship with porosity. As previously shown by Rona et al. (1998), the changes in thermal conductivity caused by variations in composition are different for the Middle Valley and TAG hydrothermal areas. Visual and thin-section observations show that many of the Middle Valley samples used for this study have a matrix rich in clay, silt, and quartz with anastomosing sulfide veins irregularly distributed throughout the sediments. These veins as well as the massive sulfide samples are composed of approximately equal amounts of pyrite and pyrrhotite. In contrast, most of the TAG samples are composed of massive pyrite and pyrite breccias with a matrix supported by anhydrite and silica (Humphris, Herzig, Miller, et al., 1996). These variations in composition are evident when comparing thermal conductivity measurements with their respective grain density values (Fig. F13A) and supports previous results (Rona et al., 1998), suggesting that matrix composition plays a significant role in the thermal conductivity of hydrothermal deposits. In particular, the presence or lack of anhydrite within the rock matrix seems to affect the measurements the most (Fig. F13A).

Porosity measurements also show different distributions between the two active hydrothermal areas. Middle Valley samples show a wide range of porosity values with relatively small changes in thermal conductivity, whereas the TAG minicores exhibit a wide range of thermal conductivities across a small range of porosity values (Fig. F13B). As discussed earlier, most of the high-porosity samples from Middle Valley are clay-rich sediments, which may explain their lower thermal conductivity. A weak trend of decreasing thermal conductivity with increasing porosity is observed for the Middle Valley samples. This trend can be

F13. Thermal conductivity variations as a function of grain density, p. 31.

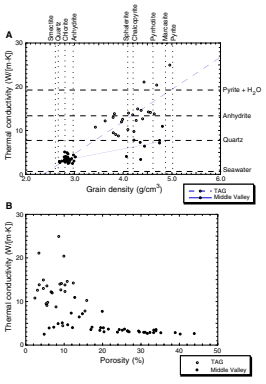

explained by the composition of the sediments, the relatively small contrast between the water and sediment grain conductivity, and perhaps increased porosity values due to water absorption by clay minerals. In contrast, visual observations and systematic changes in the grain density vs. thermal conductivity relationship (Fig. **F13A**) show that the TAG samples are mostly sulfides with large amounts of anhydrite and silica. The massive sulfide samples from Middle Valley (Table **T1**) tend to show lower porosities and their thermal conductivities fall within the lower end of the cluster encompassed by the TAG samples.

Measurement Accuracy

Thermal conductivity measurements have been previously made on sulfide samples by shipboard scientists (Davis, Mottl, Fisher, et al., 1992; Humphris, Herzig, Miller, et al., 1996; Fouquet, Zierenberg, Miller, et al., 1998), as well as by several investigators as part of their postcruise scientific analyses (Davis and Seeman, 1994; Gröschel-Becker et al., 1994; Rona et al., 1998). In these studies, two widely used techniques for measuring thermal conductivities have been the half-space needle-probe and the divided-bar methods.

Both DSDP and ODP have used the half-space needle-probe method to gather thermal conductivity data from core samples as part of the routine shipboard analyses. This method has proven to be reliable in low-conductivity formations such as sedimentary and basement samples. However, large discrepancies between the half-space needle-probe and the divided-bar methods have been recorded when measuring highly conductive materials (Davis and Seeman, 1994; Gröschel-Becker et al., 1994; Rona et al., 1998) with half-space needle-probe values systematically lower than divided-bar values (Fig. **F14A**). In contrast, the new thermal conductivity measurements of hydrothermal deposits presented here (Table **T1**) show very good agreement between the divided-bar and half-space needle-probe methods (Fig. **F14A**).

To check the accuracy of the divided-bar thermal conductivity measurements made at the Pacific Geoscience Centre (PGC), four samples were chosen for repeat measurements in laboratories located in Utah and Prague. The results show a high degree of repeatability between different laboratories (Fig. **F14B**) even though the divided-bar constructions, calibration methods, and procedures were different. In addition, the average difference between measurements is not significantly higher than the scatter of repeat measurements at each laboratory. The agreement suggests that the previous discrepancies are associated with the half-space needle-probe method.

It has been pointed out (Rona et al., 1998) that the thermal conductivity standards used for the calibration of the half-space needle-probe method are often of much lower conductivity than the measured values of the hydrothermal deposits. Because the theory for the half-space method is derived from the cylindrical geometry of the full-space method, the lack of high conductivity standards may play a significant role in accuracy of the measurements, causing fundamental differences in behavior outside the range of values delineated by the low conductivity standards. During Leg 169, the methodology of measuring half-space needle-probe thermal conductivity was changed from the old "ThermCon 85" system to a new "TK04" system.

Both systems assume that the dissipation of heat follows ideal axisymmetric behavior and calculate thermal conductivity from temperature vs. time curves as expressed by the following relationship:

F14. Thermal conductivity, divided-bar vs. half-space needle-probe method, p. 32.

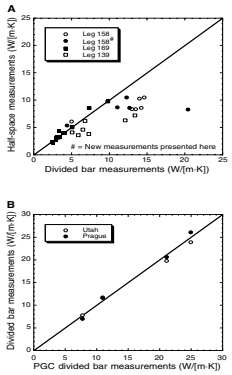

$$k_a(t) = q/4^{1/4}[\ln(t_2) - \ln(t_1)]/(T_2 - T_1),$$

where $k_a(t)$ is the apparent thermal conductivity, q is the rate at which heat flows through the material, t is the elapsed time during the measurements, and $(T_2 - T_1)$ is the steady state temperature difference between t_1 and t_2. Inaccuracies may arise from contact resistance and the finite diameter of the heat source during the early heating stage as well as from boundary effects from the source finite length and the size of the sample during the later heating stages.

The fundamental difference between these instruments lies with the dimensions of the needle and its block, and more importantly, the time over which the temperature rise during needle heating is monitored. The needle has been made smaller, and the measurement time has been reduced substantially. Previously, temperature data were used from intervals typically ranging from 60 to 240 s from initial heating (e.g., Davis, Mottl, Fisher, et al., 1992), whereas analyses using the TK04 system use data typically in an interval from 25 to 80 s (Erbas, 1985). Hence, there is a smaller chance for the finite limits of the cores to be of any consequence. The very good agreement between the Leg 169 TK04 half-space measurements and the divided-bar measurements is consistent with this conclusion (Fig. **F14A**).

DISCUSSION AND CONCLUSIONS

The process of sediment consolidation for most sedimentary environments is the result of gravitational loading from the weight of the overlying material. Over time, the overburden causes a decrease in void space as the sediment particles become more closely arranged and the pore fluids are expelled. However, the very low permeability in fine-grained sediments can slow down the process of dewatering in active tectonic environments. Such conditions may result in excess pressures in pore fluids or over pressurized zones (Taylor and Bryant, 1985). In active hydrothermal areas, pore pressures may also increase because of convective fluid circulation in the upper igneous crust beneath the relatively impermeable sediment fill and lateral tectonic stresses adding a horizontal component to the vertical loading.

In general, our results show core-scale permeabilities between 10^{-16} and 10^{-20} m^2 and fluid flow being sensitive to sulfide vein geometry. Observations from Middle Valley (Davis, Mottl, Fisher, et al., 1992; Fouquet, Zierenberg, Miller, et al., 1998) and TAG cores (Humphris, Herzig, Miller, et al., 1996) suggest that an increase in pore pressure causes hydrofracturing and sulfide mineralization along fluid conduits. Core-scale permeability measurements on Middle Valley samples show that samples with sulfide veins oriented perpendicular to the long axis of the minicore (Samples 169-856H-31R-1, 74–79 cm, and 169-1035F-11R, 6–13 cm) have lower permeabilities than samples with veins oriented parallel to the minicore axis. In these cases, preferential fluid flow is responsible for sulfide mineralization along planes of weakness that may be resulting from increased pore pressure and hydrofracturing. Fracture patterns, sulfide mineralization along veins, permeability anisotropy, and faults observed in Formation MicroScanner logs and core samples (Fig. **F1**) tend to support the idea that pore pressure is an integral component in the dynamics involving active hydrothermal systems.

The estimated in situ pressure in Hole 856H ranges from 24 MPa at seafloor to ~38 MPa at 500 mbsf (see **"Appendix,"** p. 15). As shown in

Figure F3, the low permeability and the dependence on confining pressure exhibited by several samples (i.e., Samples 4, 6, 11, and 15) suggest that the overburden pressure and consolidation within the thick sedimentary section in this area should reduce permeability significantly with depth. The permeability measurements presented here are also several orders of magnitude lower than previously reported laboratory measurements from different localities along Middle Valley (Fisher et al., 1994). Even though compositional variations between samples may have a significant effect on permeability, to a large degree, the difference in the order of magnitude between these two studies may be attributed to the difference in depth. The experiments performed by Fisher et al. (1994) were from much shallower depths than the results presented here, and the increasing overburden pressure with depth caused by the overlying sediments may have a significant effect on the amount of fluid that can flow through the sediments. A profile of permeability vs. depth (Fig. F15) shows a decrease in core-scale permeability for Middle Valley sediments to a depth approximating the base of the sulfide feeder zone at 201 mbsf. However, below this depth, three sandstones (6, 8, and 9) have the highest permeabilities recorded in Hole 856H. The lack of sulfide veins within the underlying hemipelagic and turbiditic sediments (Fouquet, Zierenberg, Miller, et al., 1998) implies that either (1) the location of Hole 856H missed most of the pervasive hydrothermal alteration and sulfide mineralization within this section; (2) there is no significant circulation of hydrothermal fluids through this unit; (3) an increase in the permeability of the sediments is reducing pore pressure, thus the probability of hydrofracturing the sediments is also decreasing; (4) the pore pressure approximates or exceeds the overburden pressure at the base of the sulfide feeder zone, allowing hydrofracturing to occur at this depth; or (5) that over pressured zones are a direct result of normal faulting and local deformation with thermal buoyancy of hydrothermal fluids playing a lesser role.

Borehole permeability and seismic experiments from Middle Valley (Becker et al., 1994; Davis and Villinger, 1992; Rohr and Schmidt, 1994) indicate that, at depth, fluid flow is controlled by large-scale fractures or faults, whereas in shallower zones, increased diffuse flow may be attributed to higher permeability and hydrofracturing caused by increased pore pressure. The results from core-scale permeability measurements in Hole 856H (Fig. F15) suggest that lithologic variations and a decrease in permeability with depth may place constraints on the depth of the sulfide feeder and massive sulfide zones found in Hole 856H (Davis, Mottl, Fisher, et al., 1992; Fouquet, Zierenberg, Miller, et al., 1998). These results indicate that perhaps the sulfide feeder zone coincides with a low permeability and high pore pressure zone where hydrofracturing is prevalent and the overburden pressure is less. Below this unit, a change in lithology and higher permeability may allow fluids to flow through the sediments, reducing the probability of hydrofracturing and subsequent sulfide mineralization. Results also show that sandstones from the turbiditic sequences have permeabilities that are two to three orders of magnitude greater than samples from shallower depths (Fig. F15). The higher permeability of these sandstones and the overall hydrothermal alteration observed in these sediments (Fouquet, Zierenberg, Miller, et al., 1998) suggest that the coarse-grained intervals within the turbiditic sequences may serve as horizontal fluid flow conduits. However, in the future, a more comprehensive study involving borehole experiments and a larger number of core measurements will be needed for determining the veracity of this hypothesis.

F15. Permeability vs. depth profile for different lithologies, p. 33.

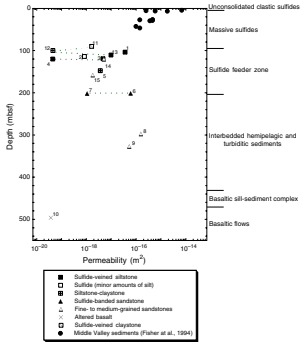

Electrical resistivity measurements are complicated by the presence of sulfide minerals. Sulfides can either cause resistivity to be frequency dependent or can cause electrical shorts on laboratory and downhole measurements, depending on vein geometry and the sulfide content. Frequency dependence is the most reliable test for the presence of or absence of sulfide minerals because data collected at a single frequency do not necessarily separate sulfide-rich cores from sulfide-free samples. From the results presented here, it is unclear whether or not resistivity measurements can discern differences in vein geometry other than producing electrical shorts when both electrodes are in direct contact with sulfide minerals. In the future, geochemical analyses should be performed in all laboratory samples for accurate determination of iron content and to further assess the reliability of complex resistivity measurements in determining sulfide content.

Thermal conductivity measurements of hydrothermally altered sediments show small variations with increasing porosity. This trend indicates that the composition of the sediments and the relatively small contrast between the water and sediment grain conductivity are the controlling factors in the conductive thermal dissipation of heat. The matrix composition of sulfide samples has a significant effect on the magnitude of thermal conductivity measurements. Overall, the presence or absence of anhydrite within the matrix seems to have a marked effect on these measurements.

Using an earlier heating time window seems to provide more accurate thermal conductivity values. Because accurate thermal conductivity measurements are required for determining heat flow from temperature measurements in the Earth and estimating thermal regimes at greater depths from near-surface temperature data, the procedure used during Leg 169 should be used in the future.

ACKNOWLEDGMENTS

Gerardo Iturrino would like to express his gratitude to Dr. Greg Boitnott of the New England Research Laboratory for his assistance and helpful comments on the electrical resistivity and permeability measurements. Gerardo Iturrino would also like to thank Dr. Gregor Eberli of the University of Miami, who provided his petrophysics laboratory for porosity and density measurements. Dr. Gilles Guerin provided insightful discussions regarding downhole electrical resistivity measurements. Dr. Andrew Fisher and Dr. Roger Morin improved this manuscript through thoughtful reviews. Ms. Diana Cutt provided helpful editorial comments to improve the quality of this manuscript. The USSSP Grant 169-F000454 supported this study.

REFERENCES

ASTM, 1989. *Annual Book of ASTM Standards for Soil and Rock: Building Stones* (Vol. 4.08): *Geotextiles:* Philadelphia (Am. Soc. Testing and Mater.).

Beck, A.E., 1957. A steady state method for the rapid measurement of the thermal conductivity of rocks. *J. Sci. Instr.,* 34:185–189.

————, 1988. Methods for determining thermal conductivity and thermal diffusivity. *In* Haenel, R., Rybach, L., and Stegena, L. (Eds.) *Handbook of Terrestrial Heat-Flow Density Determination:* Dordrecht (Kluwer Academic Publishers), 87–124.

Becker, K., Morin, R.H., and Davis, E.E., 1994. Permeabilities in the Middle Valley hydrothermal system measured with packer and flowmeter experiments. *In* Mottl, M.J., Davis, E.E., Fisher, A.T., and Slack, J.F. (Eds.), *Proc. ODP, Sci. Results,* 139: College Station, TX (Ocean Drilling Program), 613–626.

Boitnott, G.N., 1995. Permeability and complex resistivity measurements for determination of pore structure in low permeability rocks. *NSF Rep.,* DMI-9461046.

Boyce, R.E., 1973. Physical properties—methods. *In* Edgar, N.T., Saunders, J.B., et al., *Init. Repts. DSDP,* 15: Washington (U.S. Govt. Printing Office), 1115–1128.

————, 1976. Definitions and laboratory techniques of compressional sound velocity parameters and wet-water content, wet-bulk density, and porosity parameters by gravimetric and gamma-ray attenuation techniques. *In* Schlanger, S.O., Jackson, E.D., et al., *Init. Repts. DSDP,* 33: Washington (U.S. Govt. Printing Office), 931–958.

Clark, S.P., 1966. Thermal conductivity. *In* Clark, S.P. (Ed.), *Handbook of Physical Constants.* Mem.—Geol. Soc. Am., 97:461–482.

Davis, E.E., and Fisher, A.T., 1994. On the nature and consequences of hydrothermal circulation in the Middle Valley sedimented rift: inferences from geophysical and geochemical observations, Leg 139. *In* Mottl, M.J., Davis, E.E., Fisher, A.T., and Slack, J.F. (Eds.), *Proc. ODP, Sci. Results,* 139: College Station, TX (Ocean Drilling Program), 695–717.

Davis, E.E., Mottl, M.J., Fisher, A.T., et al., 1992. *Proc. ODP, Init. Repts.,* 139: College Station, TX (Ocean Drilling Program).

Davis, E.E., and Seeman, D.A., 1994. Anisotropic thermal conductivity of Pleistocene turbidite sediments of the northern Juan de Fuca Ridge. *In* Mottl, M.J., Davis, E.E., Fisher, A.T., and Slack, J.F. (Eds.), *Proc. ODP, Sci. Results,* 139: College Station, TX (Ocean Drilling Program), 559–564.

Davis, E.E., and Villinger, H., 1992. Tectonic and thermal structure of the Middle Valley sedimented rift, northern Juan de Fuca Ridge. *In* Davis, E.E., Mottl, M.J., Fisher, A.T., et al., *Proc. ODP, Init. Repts.,* 139: College Station, TX (Ocean Drilling Program), 9–41.

Erbas, K., 1985. Bestimmung der Wärmeleitfähigkeit von Festkörpern mit einer Halbraum-Linienquellen-Apparatur [M.S. thesis]. Inst. Angewandte Geophys., Techn. Univ. Berlin.

Fisher, A.T., Fischer, K., Lavoie, D., Langseth, M., and Xu, J., 1994. Geotechnical and hydrogeological properties of sediments from Middle Valley, northern Juan de Fuca Ridge. *In* Mottl, M.J., Davis, E.E., Fisher, A.T., and Slack, J.F. (Eds.), *Proc. ODP, Sci. Results,* 139: College Station, TX (Ocean Drilling Program), 627–647.

Fouquet, Y., Zierenberg, R.A., Miller, D.J., et al., 1998. *Proc. ODP, Init. Repts.,* 169: College Station, TX (Ocean Drilling Program).

Gröschel-Becker, H.M., Davis, E.E., and Franklin, J.M., 1994. Data Report: Physical properties of massive sulfide from Site 856, Middle Valley, northern Juan de Fuca Ridge. *In* Mottl, M.J., Davis, E.E., Fisher, A.T., and Slack, J.F. (Eds.), *Proc. ODP, Sci. Results,* 139: College Station, TX (Ocean Drilling Program), 721–724.

Humphris, S.E., Herzig, P.M., Miller, D.J., et al., 1996. *Proc. ODP, Init. Repts.,* 158: College Station, TX (Ocean Drilling Program).

Iturrino, G.J., Christensen, N.I., Becker, K., Boldreel, L.O., Harvey, P.K.H., and Pezard, P., 1995. Physical properties and elastic constants of upper crustal rocks from core-

log measurements in Hole 504B. *In* Erzinger, J., Becker, K., Dick, H.J.B., and Stokking, L.B. (Eds.), *Proc. ODP, Sci. Results,* 137/140: College Station, TX (Ocean Drilling Program), 273–292.

Jacobson, R.S., 1992. The impact of crustal evolution on changes of the seismic properties of the uppermost ocean crust. *Rev. Geophys.,* 30:23–42.

Johnson, G.R., and Olhoeft, G.R., 1984. Density of rocks and minerals. *In* Carmichael, R.S. (Ed.), *Handbook of Physical Properties of Rocks* (Vol. 3): Boca Raton, FL (CRC Press), 1–38.

Johnson, H.P., and Semyan, S.W., 1994. Age variation in the physical properties of oceanic basalts: implications for crustal formation and evolution. *J. Geophys. Res.,* 99:3123–3134.

Klein, J.D., Biegler, T., and Horne, M.D., 1984. Mineral interfacial processes in the method of induced polarization. *Geophysics,* 49:1105–1114.

Lees, C.H., 1892. On the thermal conductivities of crystals and other bad conductors. *Philos. Trans. R. Soc. London A,* 183:491–509.

Lockner, D.A., and Byerlee, J.D., 1985. Complex resistivity measurements of confined rock. *J. Geophys. Res.,* 90:7837–7847.

Marshall, D.J., and Madden, T.R., 1959. Induced polarization, a study of its causes. *Geophysics,* 24:790–816.

Rohr, K.M.M., and Schmidt, U., 1994. Seismic structure of Middle Valley near Sites 855-858, Leg 139, Juan de Fuca Ridge. *In* Mottl, M.J., Davis, E.E., Fisher, A.T., and Slack, J.F. (Eds.), *Proc. ODP, Sci. Results,* 139: College Station, TX (Ocean Drilling Program), 3–17.

Rona. P.A., Davis, E.E., and Ludwig, R.J., 1998. Thermal properties of TAG hydrothermal precipitates, Mid-Atlantic Ridge: a comparison with Middle Valley, Juan de Fuca Ridge. *In* Herzig, P.M., Humphris, S.E., Miller, D.J., and Zierenberg, R.A. (Eds.), *Proc. ODP, Sci. Results,* 158: College Station, TX (Ocean Drilling Program), 329–335.

Sclater, J.G., Jaupart, C., and Galson, D., 1980. The heat flow through oceanic and continental crust and the heat loss of the Earth. *Rev. Geophys. Space Phys.,* 18:269–311.

Stein, C.A., and Stein, S., 1994. Constraints on hydrothermal heat flux through the oceanic lithosphere from global heat flow. *J. Geophys. Res.,* 99:3081–3095.

Taylor, E., and Bryant, W.R., 1985. Geotechnical properties of sediments from the Middle America Trench and slope. *In* von Huene, R., Aubouin, J., et al., *Init. Repts. DSDP,* 84: Washington (U.S. Govt. Printing Office), 745–766.

Thompson, G., 1983. Basalt-seawater interaction. *In* Rona, P.A., Boström, K., Laubier, L., and Smith, K.L., Jr. (Eds.), *Hydrothermal Processes at Seafloor Spreading Centers:* New York (Plenum), 225–278.

Wong, J., 1979. An electrochemical model of the induced-polarization phenomenon in disseminated sulfide ores. *Geophysics,* 44:1245–1265.

APPENDIX

Methodology

Index properties were measured on vertical and horizontal minicores (2.54 cm in diameter and 2.54–3.81 cm in length) from Middle Valley at the petrophysics laboratory of the Rosenstiel School of Marine and Atmospheric Sciences in Miami, Florida (Table T1). All samples are labeled using the conventional ODP system of leg-hole-core-section-interval (e.g., Sample 169-856H-65R-2, 71–73 cm) with a letter "h" (horizontal or perpendicular to axis of the borehole) or "v" (vertical or parallel to the borehole) added to indicate the orientation of the minicore.

Wet and dry sample weights and volumes were determined using a microbalance for measuring mass (±0.002 g accuracy) and a pycnometer for measuring sample volumes (±0.03%). The pycnometer is specifically designed to measure sample volume and to provide the necessary information to calculate the density, porosity, and water content of the samples by employing Archimedes' principle of fluid displacement. The displaced fluid is helium, which assures penetration into crevices and pore spaces approaching 1 Å (10^{-10} m). Purge times of 5 min were used to approach a helium-saturated steady-state condition. After measuring the wet weights, samples were dried at 100°C for a period of 24 hr to drive off water. The determination of water content followed the methods of the American Society for Testing and Materials (ASTM) designation (D) 2216 (ASTM, 1989). As outlined in the ASTM D2216, corrections are required for salt when measuring marine samples. Samples were saturated in seawater and placed in a vacuum for 24 hr to achieve in situ wet conditions. All measurements were corrected for salt assuming a pore-water salinity of 35‰. This method was then used to calculate both bulk density and porosity values.

Index properties were calculated in a fashion similar to that described in Boyce (1973, 1976) and Iturrino et al. (1995). The techniques are also described below for convenience and clarity of the methods. Bulk density (ρ_b) is the density of the whole sample, including the pore fluid, and is given by

$$\rho_b = M_t / V_t, \quad (1)$$

where M_t = total mass (saturated) and V_t = saturated sample volume. The total mass (M_t) was measured using the electronic balance and the total volume was calculated using the mass of the pore fluid (M_w), the volume of the pore fluid (V_w), and the mass of the dry sample as expressed by the following equation:

$$M_w = (M_t - M_d)/s, \quad (2)$$

where M_d = dry sample mass, s = salt factor = (1 – r) = 0.965, and r = salinity = 0.035. This allows the calculation of the pore-water volume (V_w),

$$V_w = M_w/\rho_w, \quad (3)$$

where ρ_w = density of pore water = 1.0245 g/cm³. The total wet volume (V_w) was then calculated using the following equation:

$$V_t = V_w + V_d, \quad (4)$$

where V_d = dry sample volume, thus permitting the direct calculation of bulk density values using Equation 1. Grain densities (ρ_g) were calculated with the following equation:

$$\rho_g = M_d/V_d. \quad (5)$$

Overall, accuracies in density determinations are ~0.2% or 0.01 g/cm³. The porosity (ϕ) was calculated using the expression

$$\phi = [M_w/(V_t\, \rho_w)] \cdot 100. \quad (6)$$

Porosity values were determined to approximately ±0.2%, assuming that the porosity is interconnected and fluid saturated. The results from 14 samples were cross checked with similar measurements made on the same samples at the New England Research (NER) Laboratory in Junction City, Vermont. Results from these measurements (Table **T1**) show a standard deviation of 0.076 g/cm³ for grain density values and 2.46% for porosity determinations. The largest variations in these measurements were associated with samples having clay-rich mineralogy and may be due to absorbed water retained by the clays.

A total of 15 samples was chosen for making permeability and electrical resistivity measurements as a function of confining pressure at the NER Laboratory. All measurements made as a function of pressure were obtained at a constant pore pressure (P_p) of 5 MPa and confining pressures (P_c) ranging from 10 to 50 MPa. Assuming an average density of 3.0 g/cm³ and a water depth of 2400 m, the estimated in situ pressure for Hole 856H at 500 mbsf is 38 MPa. In contrast, in situ pressure conditions at the bottom of Hole 857D, approximately located 1.6 km northwest of the Bent Hill area (Davis, Mottl, Fisher, et al., 1992), would be 46 MPa for a 936 mbsf section, 2400-m water depth, and an average density of 2.5 g/cm³. Therefore, the 50-MPa upper limit was chosen for estimating maximum in situ conditions for boreholes drilled along Middle Valley where the maximum effective pressure (P_e) for all the measurements would be ~45 MPa ($P_e = P_c - P_p$).

Values of permeability were obtained using pore pressure transients and inferred from the downstream pore pressure response to a change in upstream pore pressure (Boitnott, 1995). Out of a total of 15 samples, two (Samples 169-856H-65R-2, 71–73 cm, and 169-1035F-11R-1, 6–13 cm) had permeabilities too low to be accurately measured with the pore pressure transient. For these two cores a pulse decay transient was used, and permeability was only obtained at a single confining pressure of 10 MPa (Boitnott, 1995). The results of the permeability experiments are shown in Table **T2.**

Electrical properties were measured with a four-electrode assembly arranged for low-frequency measurements in the range of 20 mHz to 100 kHz (Boitnott, 1995). Electrical impedance was measured over a frequency range from 20 mHz to 100 kHz using a four-electrode technique (Lockner and Byerlee, 1985). Current and voltage electrodes were separated from one another at each end of the core to minimize electrode impedance (Boitnott, 1995). A computer-controlled function generator provided the input to a circuit consisting of a switchable reference resistor in series with the sample. Two matched Field Effect Transistors input amplifiers measured the voltage across the reference resistor and the

sample. A digital oscilloscope recorded the signals from these amplifiers. The amplitude ratio and phase shift between the two signals was used to measure the complex electrical impedance of the sample. Integrated computer control of the function generator and the oscilloscope allowed for automated sweeps through user-defined frequency ranges in a single capture. Measurements were made using two different four-electrode configurations. The change in methodology was necessary for cores with continuous sections of interconnecting sulfides. The methods used were (1) method 1, voltage electrodes directly touch each end of the core; and (2) method 2, a thin polyester screen is inserted between each voltage electrode and the core. These nonconducting screens provided a small gap between the voltage electrodes and the core. This technique allowed ionic conduction through a small layer of pore fluid instead of the traditional direct contact current conduction from electrode to electrode. Resistivity measurements were made with the core samples saturated in a 0.10-M sodium chloride solution with a fluid conductivity of 10 mS/cm. Brine conductivity was measured separately at the start of each experiment. All electrical resistivity measurements are shown in Table **T2.**

Thermal conductivity measurements were performed on 50 samples using the divided-bar apparatus from the Pacific Geoscience Centre (PGC), and the results are shown in Table **T1.** The apparatus consists of two constant temperature baths at the top and bottom of a composite cylindrical bar comprising the sample bracketed symmetrically by a pair of copper measurement discs. In addition, the system has a pair of standard discs and a second pair of copper measurement discs (Lees, 1892; Beck, 1957, 1988; Davis and Seeman, 1994). The baths maintain a 10°C temperature difference that is adjusted to evenly span the ambient laboratory temperature of typically 20°C. The exterior surface of the composite bar is insulated to reduce radial heat loss and to ensure constant heat flow along the axis of the bar. After an equilibration period of 15–20 min, the thermal resistance of a sample is determined simply by comparing the temperature drop across the sample to that across either the upper or lower standard disc. Comparison of the temperature drops across the two standards provides verification of the consistency of heat flow along the length of the bar and that the radial heat loss is not a significant source of error. Using similar systems, duplicate thermal conductivity measurements were also performed on four samples at the Geophysical Institute of the Czech Academy of Sciences in Prague and the Department of Geology and Geophysics of the University of Utah in Salt Lake City, Utah, for comparison with the PGC results (Table **T3**).

Thin sections from the end billets of the minicores were made for the 15 samples where permeability and electrical resistivity measurements were made. Descriptions of these samples were based on thin-section observations, whereas the remaining sample descriptions were based on visual observations of the core faces. Even though temperature effects may alter electrical resistivity, and to some degree the permeability and thermal conductivity measurements, they were not considered in this study.

Figure F1. Formation MicroScanner (FMS) log and core data from Hole 856H in the Bent Hill area of Middle Valley. **A.** Depth scale in meters below seafloor (mbsf), core recovery, and stratigraphic and log units from this hole are shown for reference (see Fouquet, Zierenberg, Miller, et al., 1998). **B.** Section of the FMS logs from the sulfide feeder zone showing fracture patterns. Pad numbers 1–4 are given at the top of the figure. **C.** Core photograph showing a subvertical massive sulfide vein and several other sulfide veins crosscutting hydrothermally altered sedimentary rock. Correlation of this piece with the FMS data (pad 4) suggests that the approximate depth corresponds to the area within the box shown in view B. **D.** FMS section of the layered sediments showing a series of steeply dipping fractures with a west-northwest trend. **E.** The bottommost pillow basalts. (**Figure shown on next page.**)

Figure F1. (Caption on previous page.)

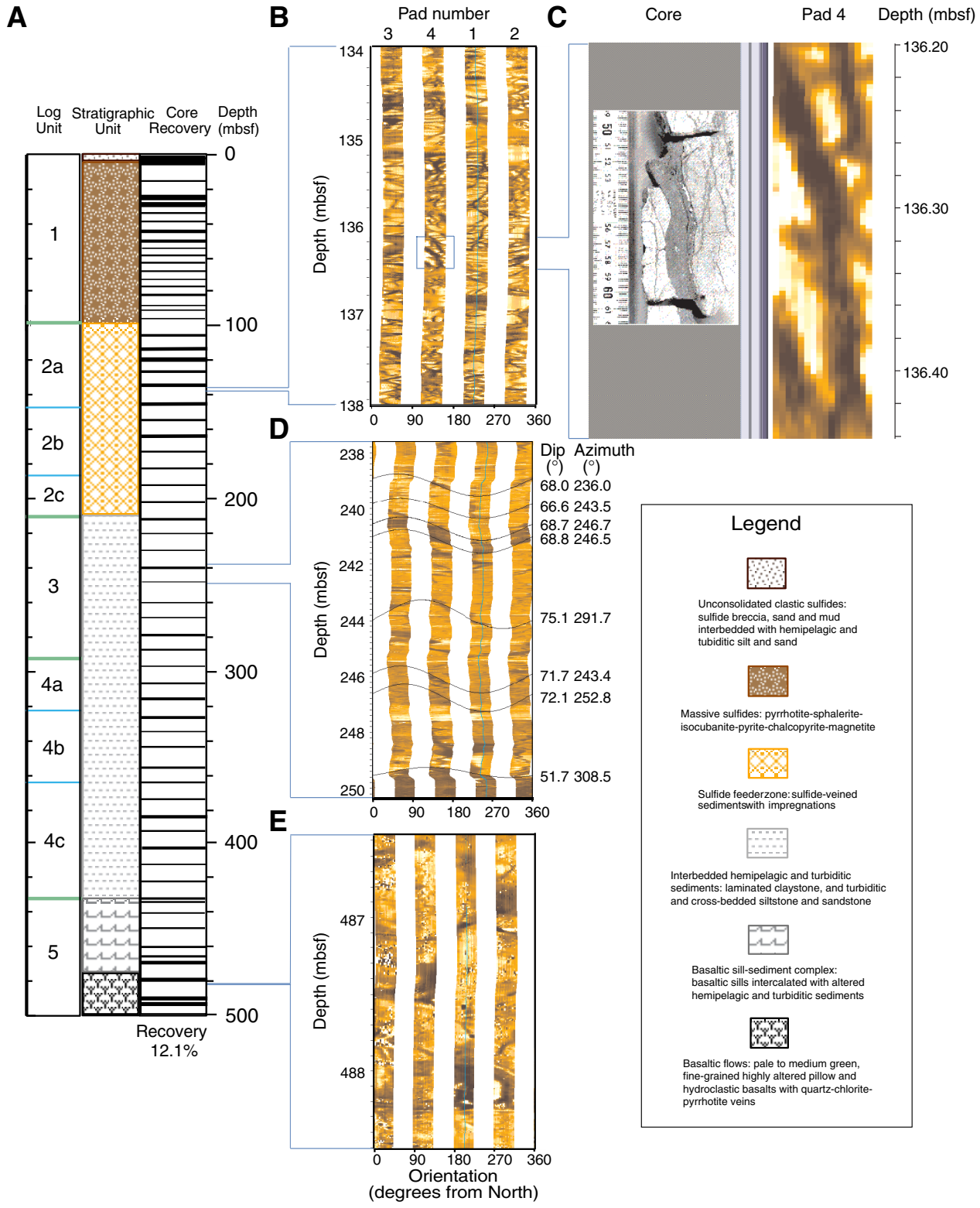

Figure F2. Northwest to southeast schematic cross section of the active Trans-Atlantic Geotraverse (TAG) hydrothermal mound. The flow patterns within the mound are derived from the mineralogy and chemistry of the deposits and the chemistry of white smoker and black smoker fluids. Also shown is a schematic lithostratigraphy of the TAG hydrothermal mound from rocks recovered from the same northwest-southeast transect of the TAG-1, TAG-2, and TAG-4 areas. The holes in each area were drilled in close proximity to each other (10–15 m) and their stratigraphy has been considered together to form a composite section at each location. Percentages of core recovery are also given at the bottom of each composite column (modified from Humphris, Herzig, Miller, et al., 1996).

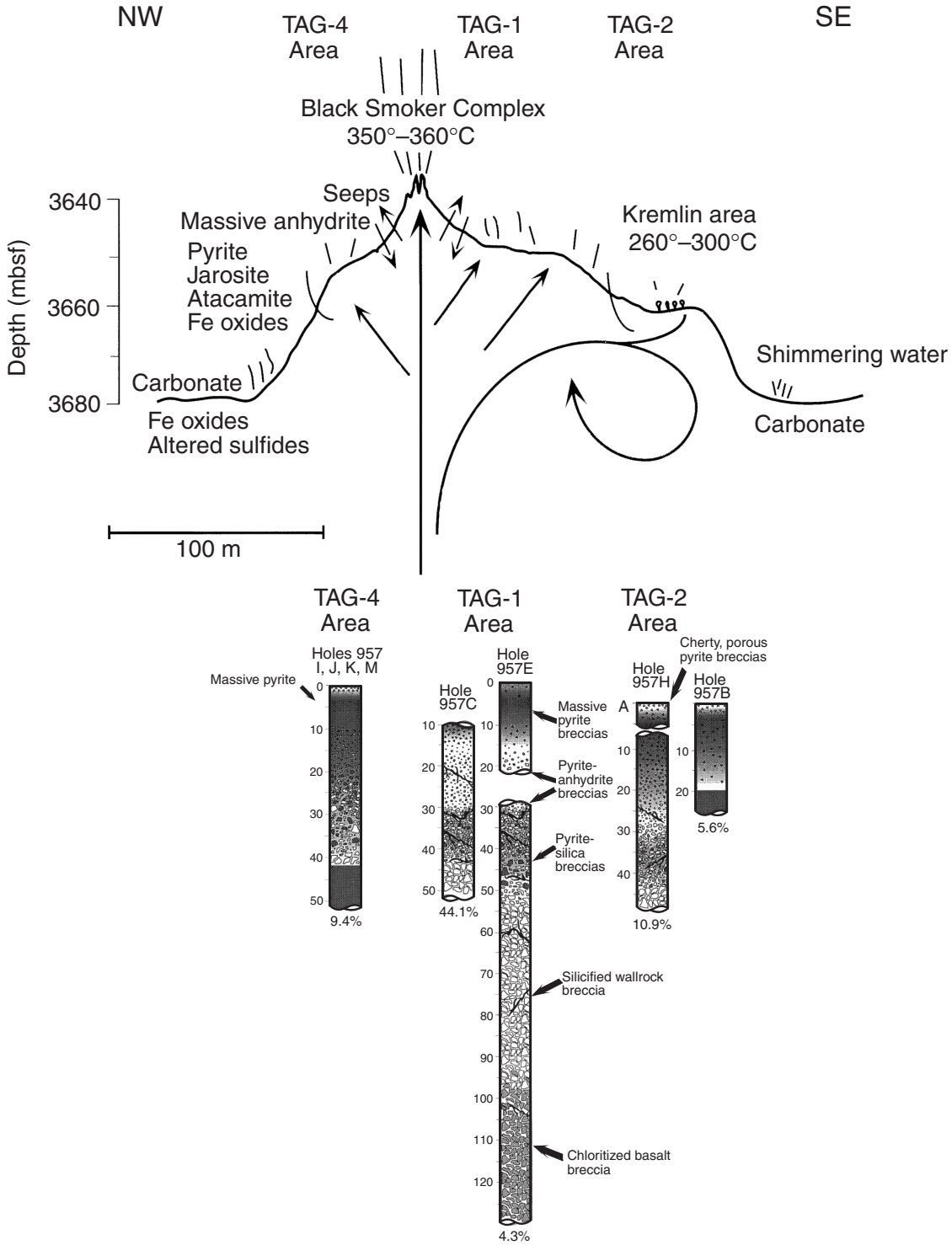

Figure F3. Permeability measurements as a function of confining pressure. Pore pressure remained constant at 5 MPa for all experiments. **A.** Permeability measurements plotted in a logarithmic scale for all 15 samples as a function of upgoing pressure values. **B.** Selected examples of recoverable and nonrecoverable permeability caused by sediment deformation during high-pressure experiments. Numbers represent samples as listed in Table T2, p. 36. Arrows shows the direction of upgoing and downgoing pressure intervals.

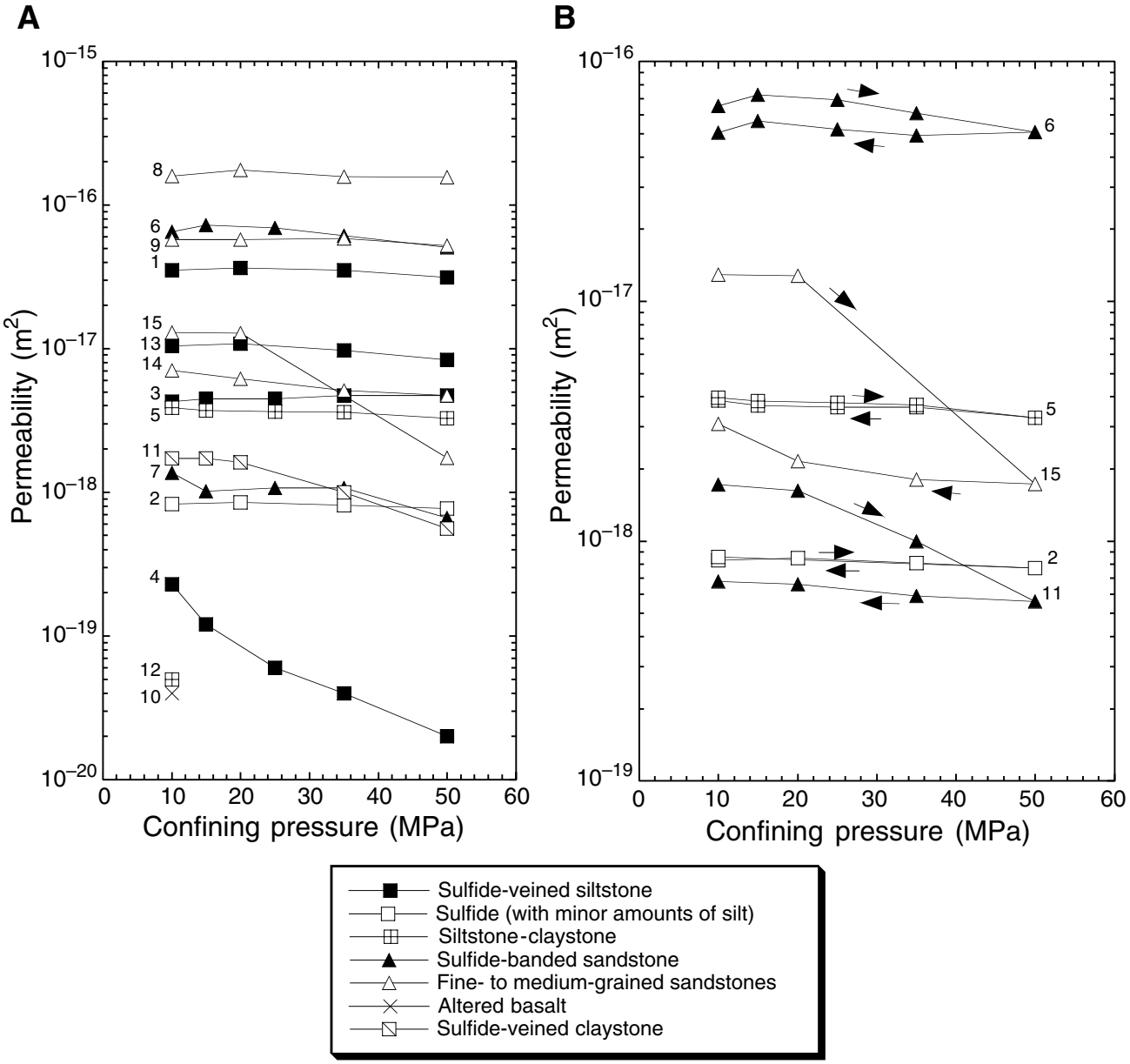

Figure F4. Correlation between log permeability (k) and log porosity (ϕ) measurements for Middle Valley samples. Permeability measurements, plotted at 10 MPa confining pressure and 5 MPa pore pressure, are from the beginning of the experiments before permanent sediment deformation was observed. Numbers represent samples as listed in Table T2, p. 36. A least-squares line illustrates the general trend.

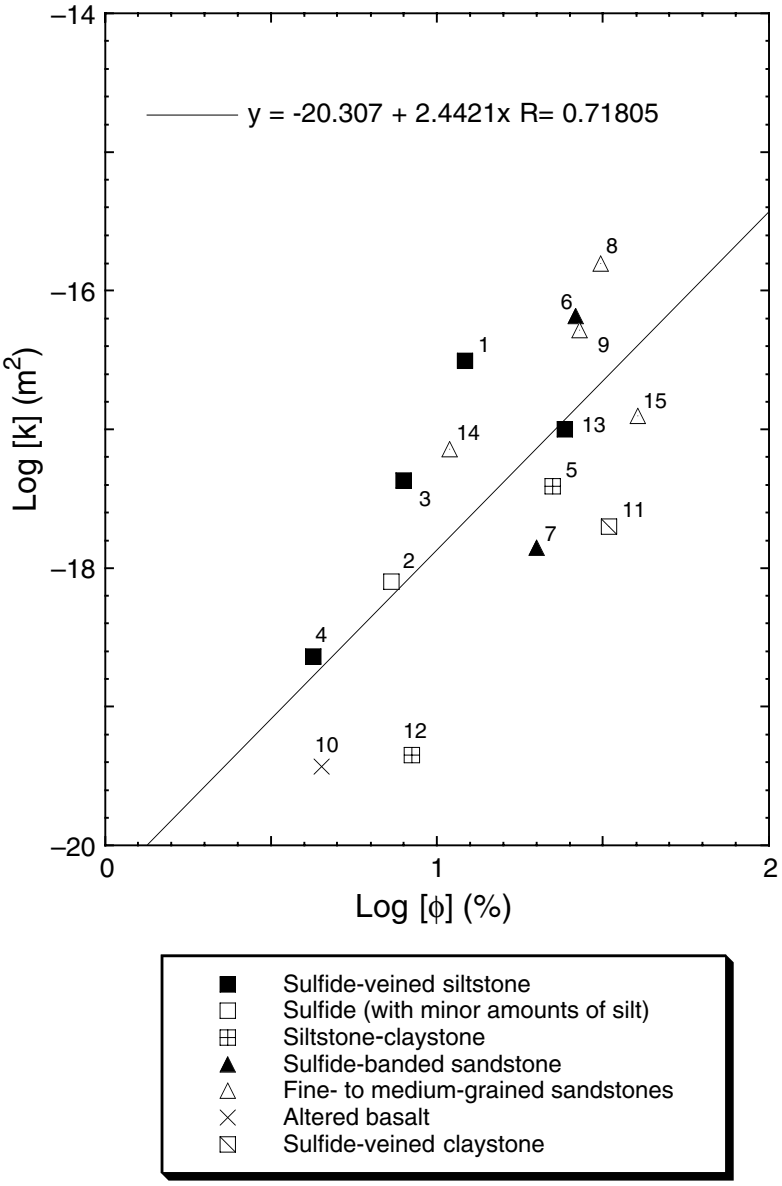

Figure F5. **A.** Comparison between grain density and permeability measurements made at 10 MPa confining pressure and 5 MPa pore pressure. **B.** Relationship between grain density and porosity measurements measured at atmospheric pressure. Grain densities for mineral assemblages commonly found in these rocks are also plotted for showing variations with increasing sulfide content (from Johnson and Olhoeft, 1984). Numbers represent samples as listed in Table T2, p. 36.

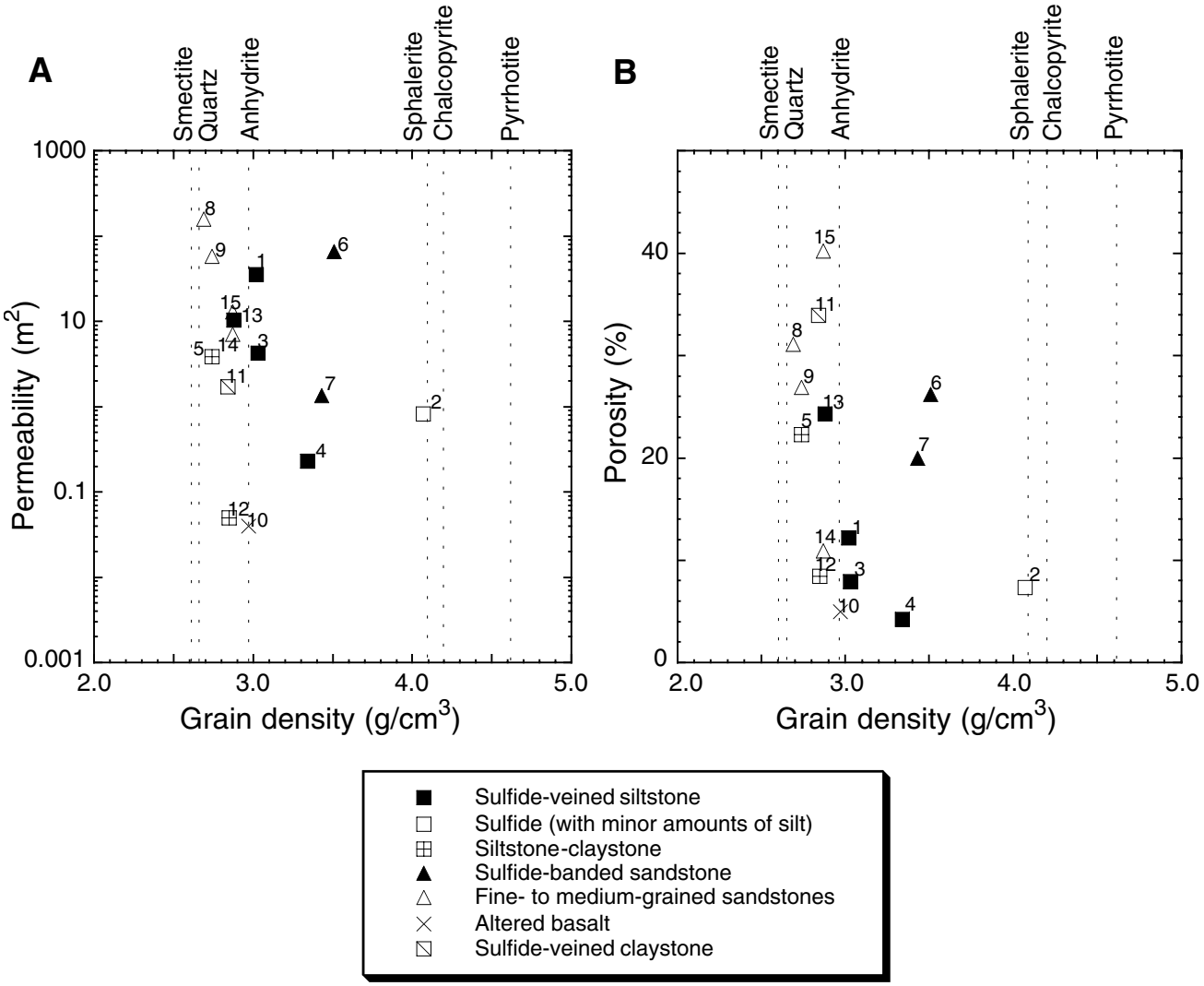

Figure F6. Permeability anisotropy measurements made on a limited set of samples at 10 MPa confining pressure and 5 MPa pore pressure. Permeability values are plotted in a logarithmic scale. Numbers represent samples as listed in Table T2, p. 36.

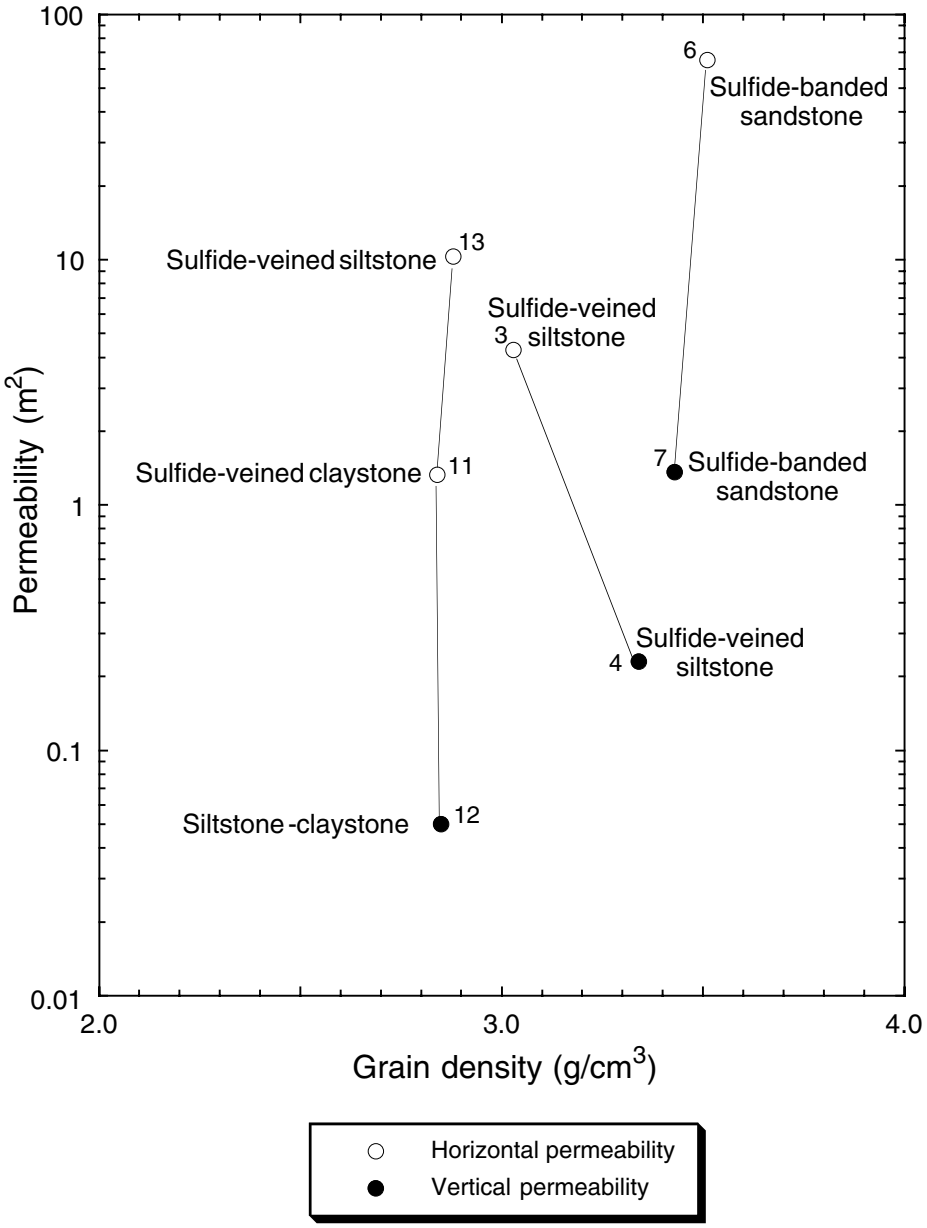

Figure F7. Formation factor measurements plotted as a function of confining pressure in a logarithmic scale. Data from 12 samples are plotted showing method 2 resistivity and only upgoing pressure values are used for clarity of the display. Numbers represent samples as listed in Table T2, p. 36.

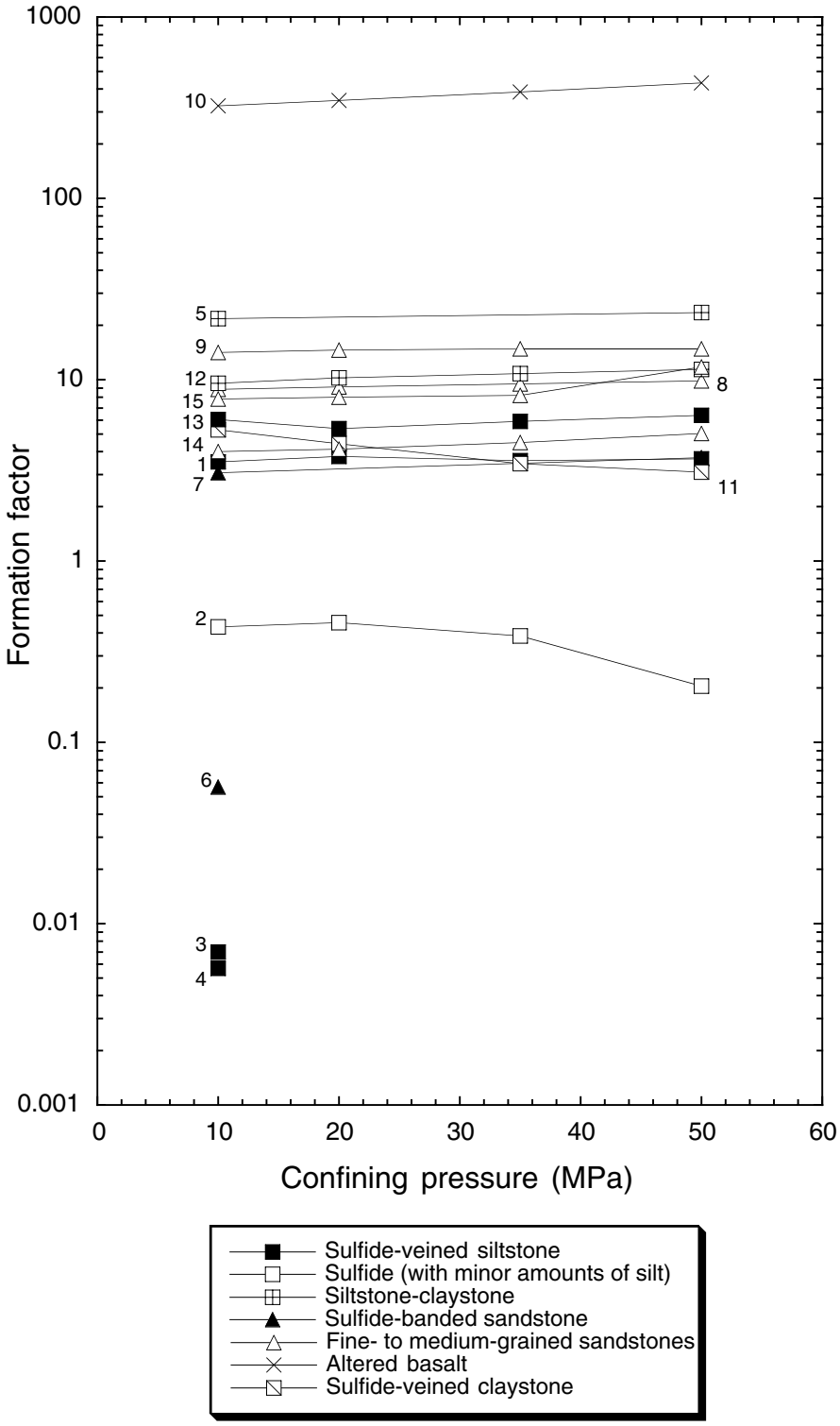

Figure F8. Relationship between permeability and formation factor as a function of confining pressure. Most samples show that as the confining pressure increases, formation factor values increase slightly with decreasing permeability. However, two samples do not follow this trend (Samples 169-856H-21R-1, 78–80 cm, and 169-1035F-10R-1, 25–27 cm). Numbers represent samples as listed in Table T2, p. 36.

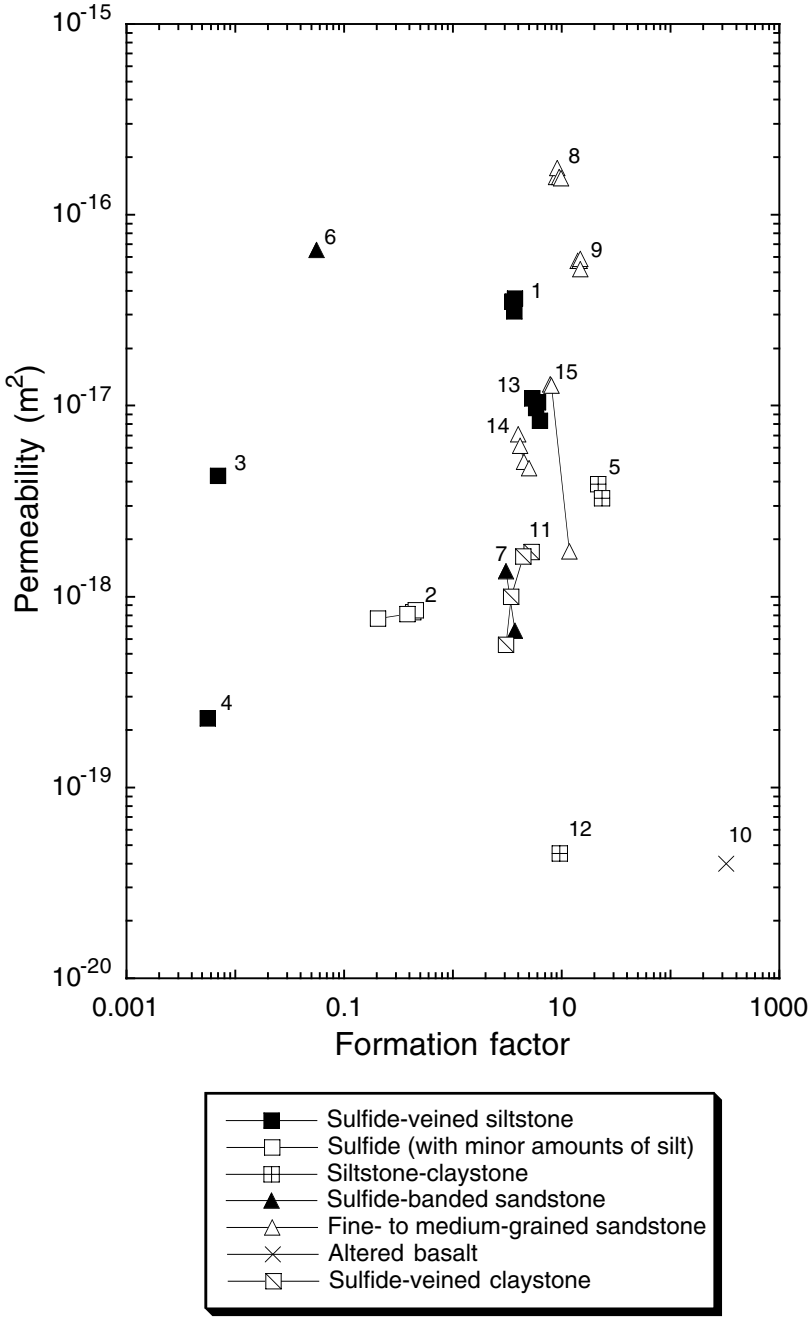

Figure F9. Relationship between formation factor (FF) and frequency [f] from measurements obtained with method 2 (see "Appendix," p. 15). Data from 12 samples was taken from a single resistivity capture at 10 MPa confining pressure and 5 MPa pore pressure. Numbers represent samples as listed in Table T2, p. 36.

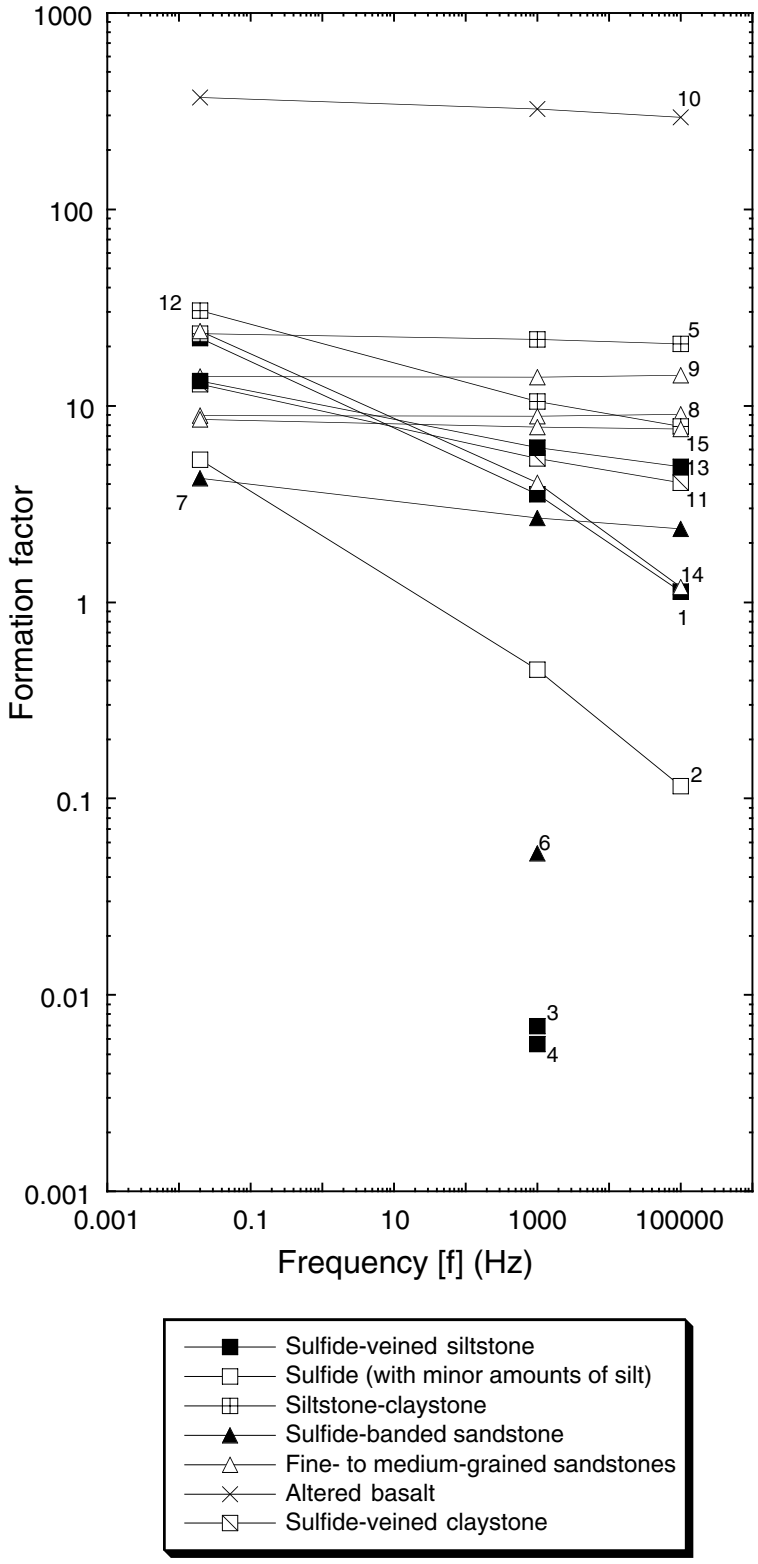

Figure F10. A. Comparison between formation factor (FF) and grain density as a function of frequency. Grain densities for mineral assemblages commonly found in these rocks are also plotted (from Johnson and Olhoeft, 1984). **B.** Relationship between formation factor and porosity as a function of frequency. Cores with high sulfide content tend to have lower porosity values and higher frequency dependence. Numbers represent samples as listed in Table T2, p. 36.

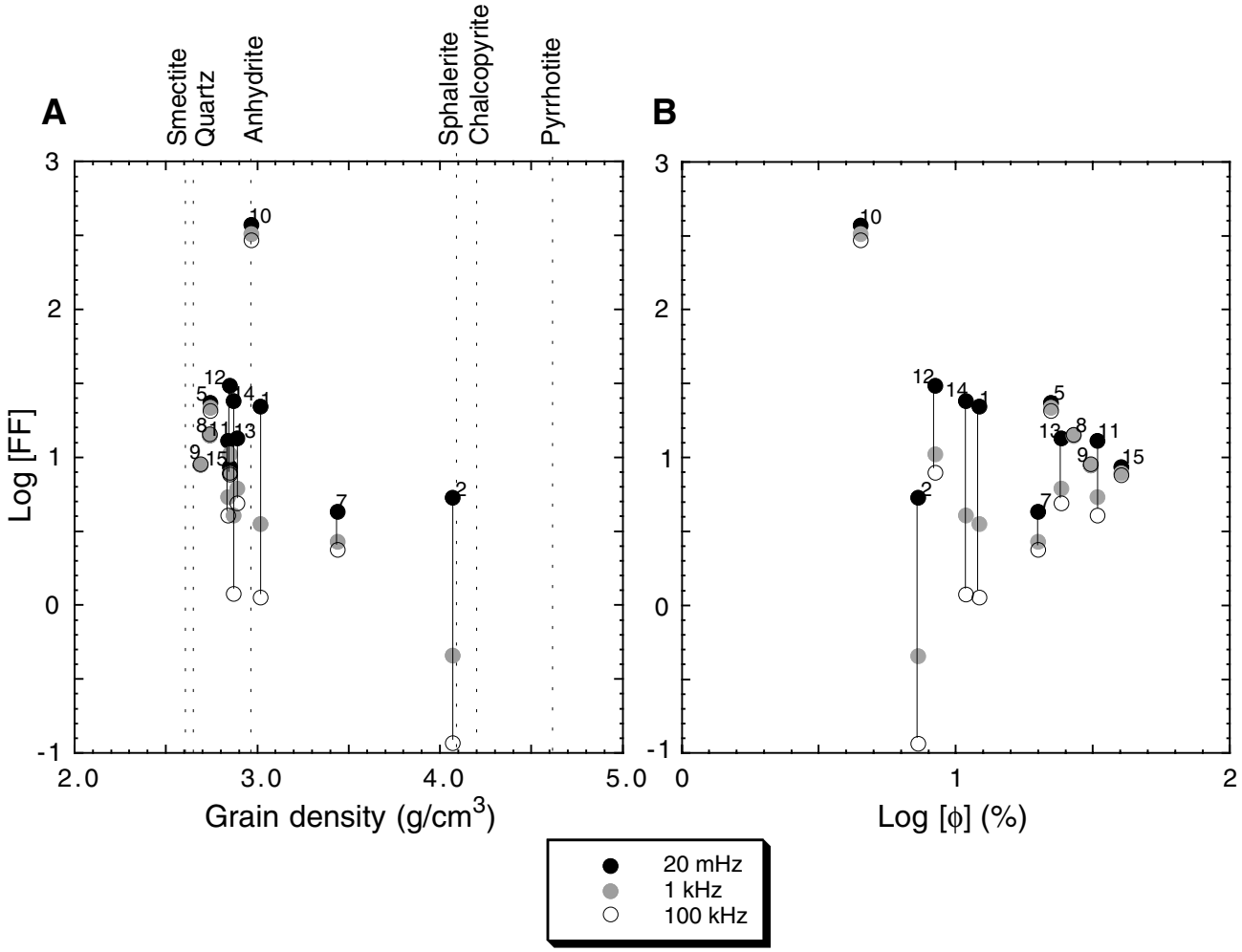

Figure F11. Relationship between sample and fluid conductivities measured on Sample 169-856H-25R-3, 16–18 cm. A least-squares fit illustrates the trend.

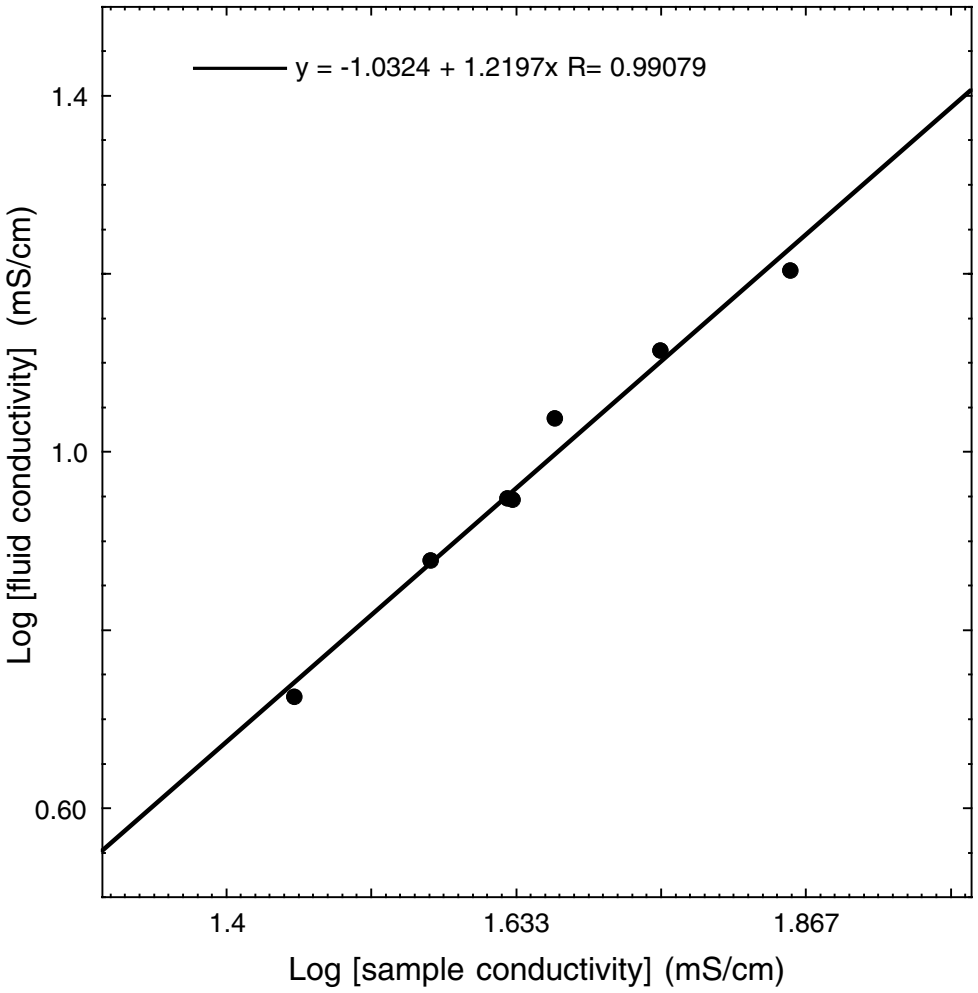

Figure F12. A. Resistivity measurements obtained from Sample 169-1035F-12R-1, 132–134 cm, using methods 1 and 2 described in the text. The dotted line represents method 1, whereas the solid line is method 2. Representations of the real and the negative of the imaginary components of resistivity are expressed as solid and open circles, respectively. **B.** Frequency dependence of resistivity for Sample 169-856H-21R-1, 78–80 cm, using method 2 in which a thin screen separates the sample from the voltage electrodes. Fluid conductivity is 9.94 mS/cm. **C.** The same relationship as in view B, but using method 1 in which the sample touches the voltage electrodes. Resistance is ~0.1 Ω. **D.** Complex resistance of the electrodes where two thin polyester screens separated the voltage electrodes and no sample was present. The distance between the electrodes was estimated to be less than 100 µm with no confining pressure. As with the other examples, measurements were made at 10 MPa confining pressure and 5 MPa pore pressure. The resistance at 0.02 Hz is 7.2 Ω and it is interpreted to be caused by electrochemical reactions between brine and electrodes, as well as electrode capacitance. Brine conductivity is 11.22 mS/cm.

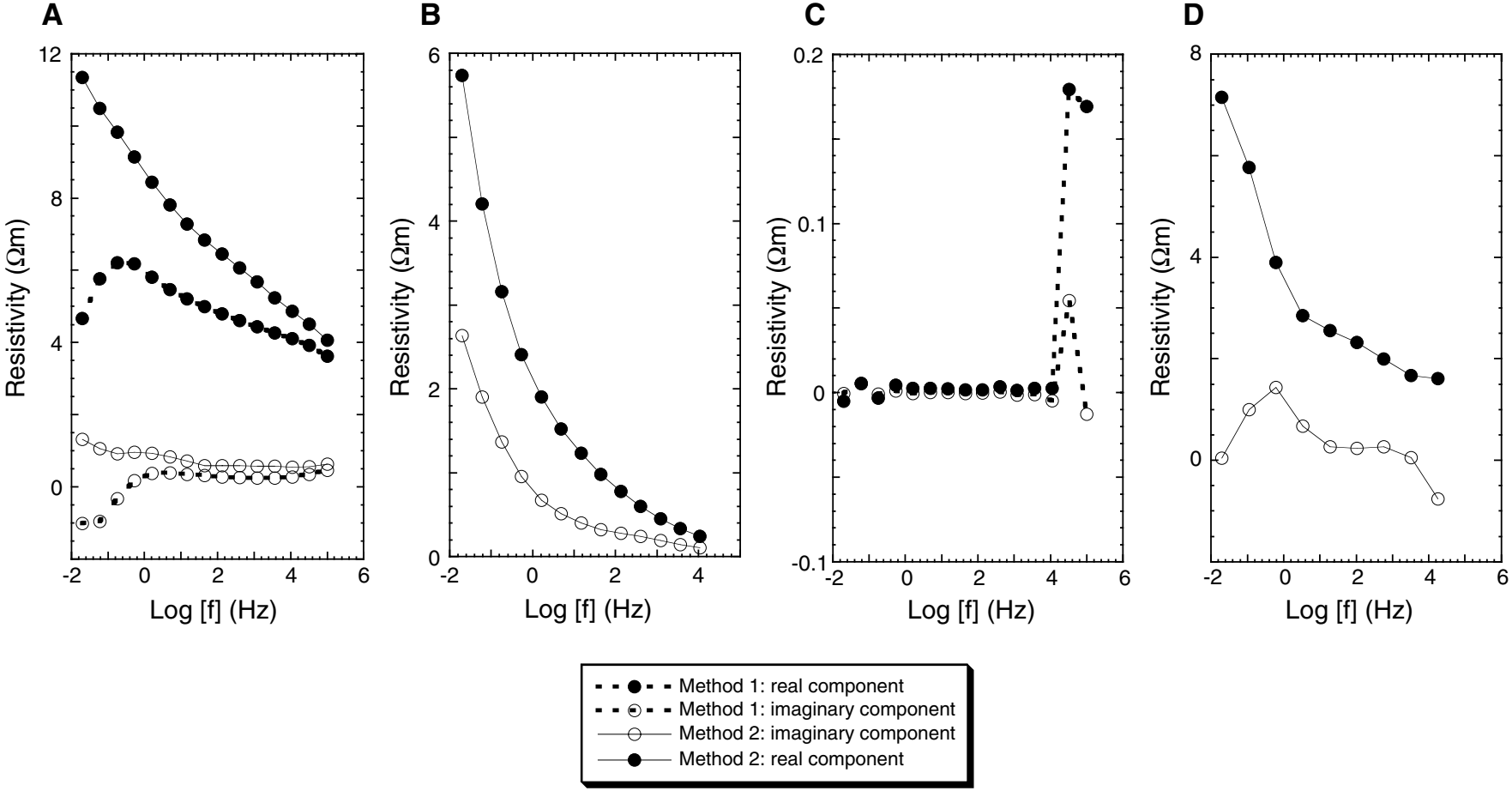

Figure F13. A. Thermal conductivity variations as a function of grain density plotted for hydrothermal deposits from the Middle Valley and Trans-Atlantic Geotraverse (TAG) hydrothermal areas. Thermal conductivity measurements for single mineral aggregates from Clark (1966) and mineral grain densities from Johnson and Olhoeft (1984) are also plotted for illustrating the difference between the sulfide deposits and the sediments. **B.** Thermal conductivity variations as a function of porosity for Middle Valley and TAG samples. Data from the TAG area presented in both figures are from Rona et al. (1998) and new values presented here, whereas all Middle Valley values are from this study.

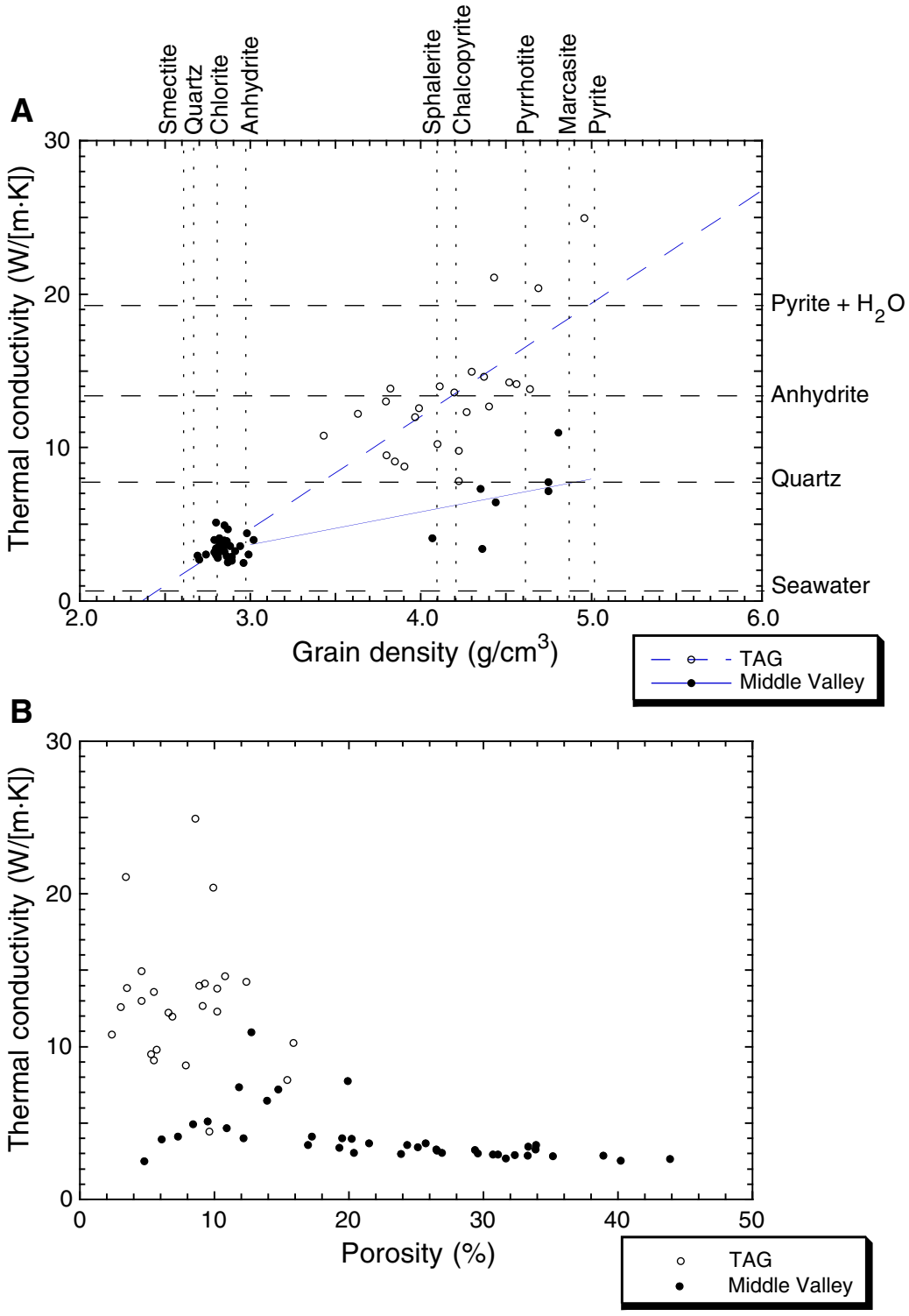

Figure F14. A. Thermal conductivity measurements gathered with the divided-bar method plotted against the same measurements obtained with the half-space needle-probe method. Divided-bar measurements were from a 2.54-cm minicore obtained from the same piece that the half-space needle-probe measurements were collected. Data from Legs 139 (Gröschel-Becker, et al., 1994), 158 (Rona et al., 1998; new data presented here), and 169 (new data presented here) are shown. Notice the good correlation between the Leg 169 measurements and the discrepancies in the Legs 139 and 158 data. Line represents a 1:1 correlation between methods. **B.** A comparison between the divided-bar measurements performed at the Pacific Geoscience Centre (PGC) and the same measurements performed on the same samples at Utah and Prague.

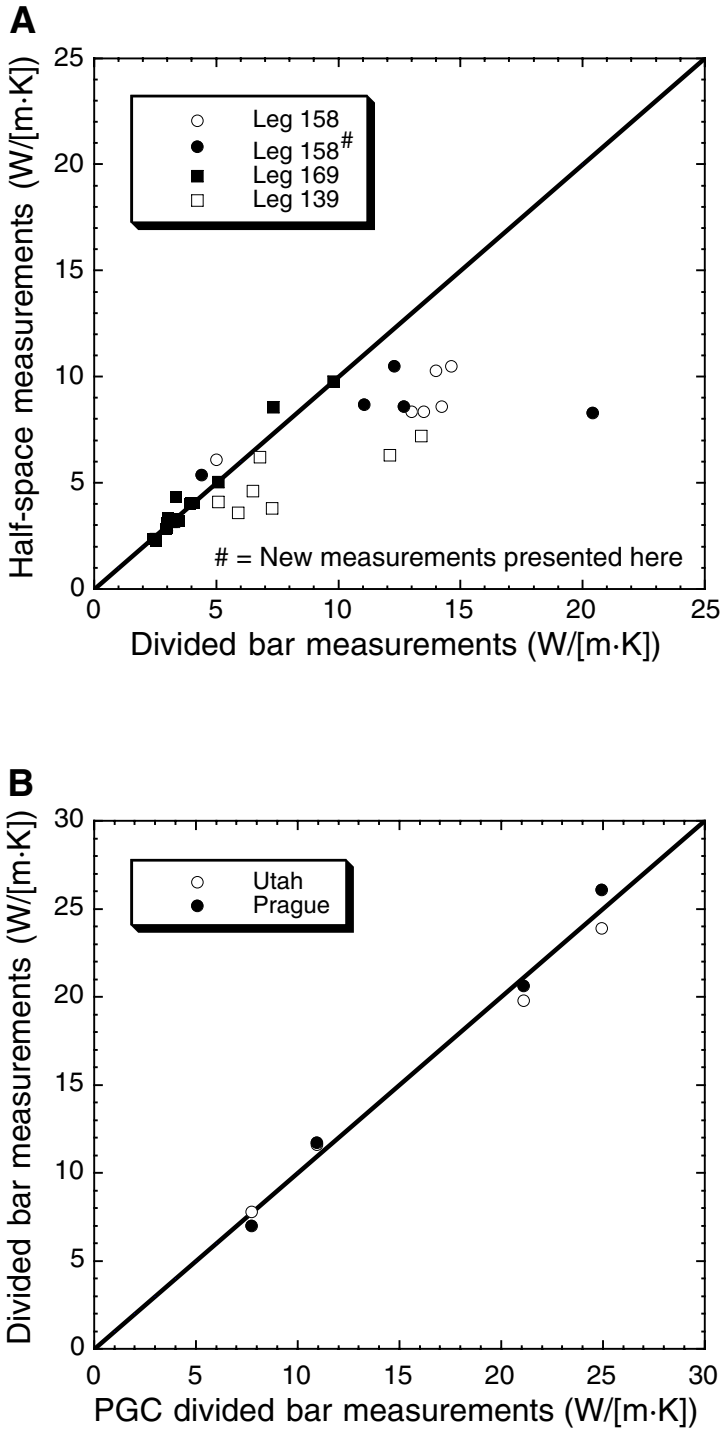

Figure F15. Permeability vs. depth profile for different lithologies from Middle Valley. All the permeability values are assumed to approximate in situ conditions based on sample depth estimates, water depth, and the effect of the overlying sedimentary section (see "Appendix," p. 15). Dashed lines are used to illustrate that the vertically oriented samples (4, 6, and 12) have lower permeabilities than their respective adjacent horizontal pairs (3, 7, and 11–13). Samples from Fisher et al. (1994) are from the Bent Hill and Dead Dog active venting areas of Middle Valley and illustrate the systematic core-scale permeability changes with depth in this area. Lithostratigraphic boundaries from Hole 856H are also shown for reference.

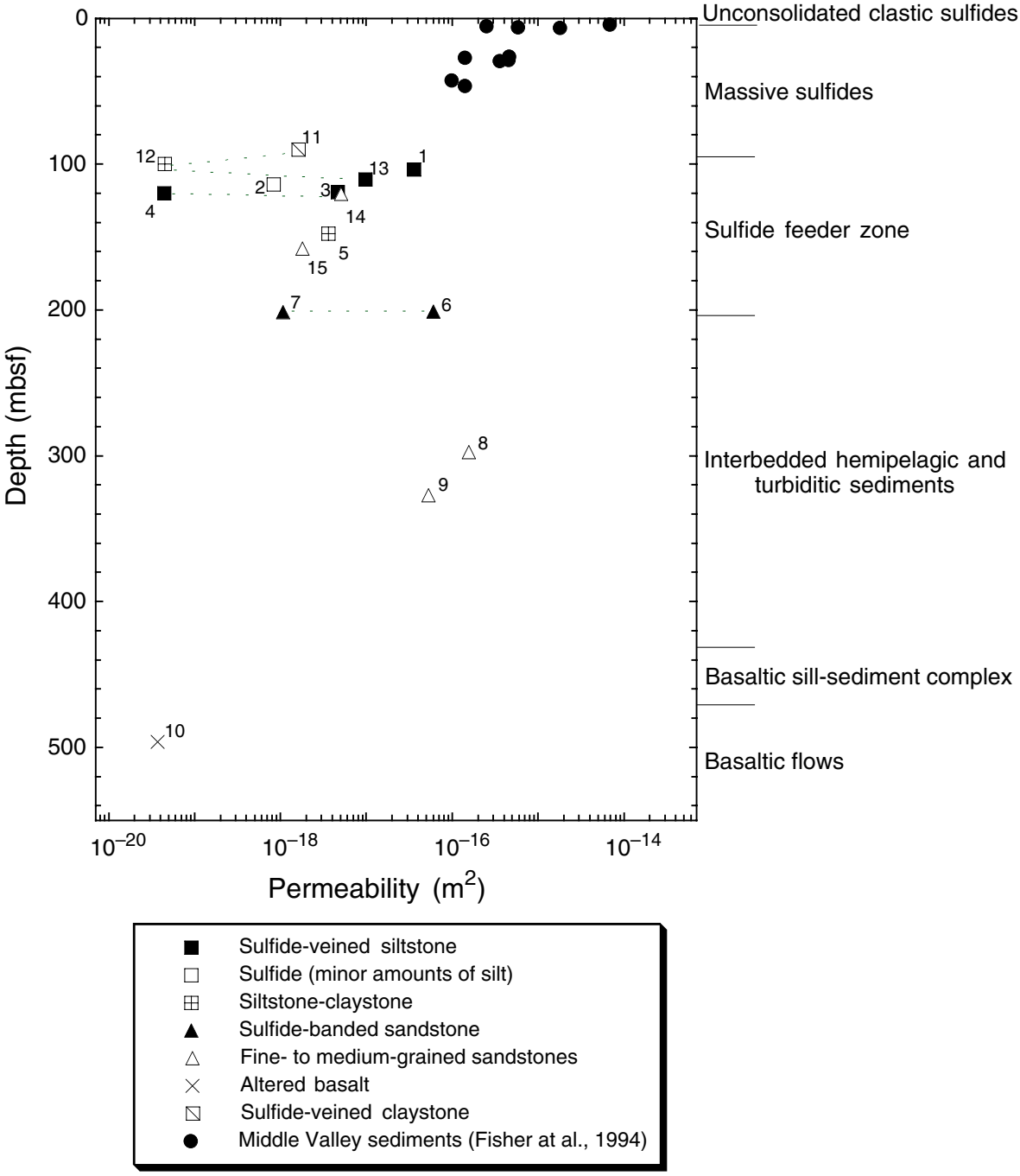

Table T1. Index properties and thermal conductivities of samples from the Middle Valley and TAG hydrothermal areas. (See table notes. Continued on next page.)

Core, section, interval, cm	Orientation[1]	Piece number	Depth[2] (mbsf)	Bulk density (g/cm³)	Grain density[3] (g/cm³)	Pore-water volume (cm³)	Porosity[3] (%)	Thermal conductivity[4] (W/[m·K])	Lithology and comments
169-856H-									
20R-1, 22-24	h	3A	103.82	2.77	3.02 (3.04)	1.31	12.18 (12.50)	3.98	Sulfide-veined siltstone; electrical short from one large sulfide vein
21R-1, 78-80	h	5E	114.18	3.85	4.07 (4.02)	0.97	7.31 (6.60)	4.11	Sulfide sample from a sulfide-veined siltstone unit; electrical short; crack porosity present
22R-2, 65-67	h	8	119.25	2.87	3.03 (2.99)	0.86	7.93 (7.90)	NA	Sulfide-veined siltstone; electrical short from many sulfide veins
22R-2, 124-130	v	15	119.84	3.24	3.34 (3.34)	1.06	4.25 (4.58)	NA	Sulfide-veined siltstone; electrical short from one large sulfide vein; disseminated sulfides
24R-1, 25-27	h	2A	133.95	3.52	3.96	2.06	14.87	NA	Sulfide-veined mudstone
25R-3, 16-18	h		147.96	2.13	2.74 (2.74)	2.55	22.30 (22.30)	NA	Silt and clay matrix with disseminated sulfide grains
27R-1, 21-23	h		162.71	2.23	2.86	3.48	33.52	NA	Siltstone with minor sulfides
29R-1, 55-57	h	9	182.25	2.20	2.80	4.66	33.36	3.45	Siltstone with minor sulfides
31R-1, 9-11	h	2	201.09	2.85	3.51	3.78	26.19	NA	Sulfide-banded sandstone; electrical short from large sulfide vein parallel to minicore axis
31R-1, 74-79	v	10	201.74	2.95	3.43 (3.27)	4.50	19.94 (16.4)	NA	Sulfide-banded sandstone; wide sulfide veins perpendicular to minicore axis
32R-1, 53-55	h	9A	211.13	2.63	2.80	1.09	9.49	5.10	Fine-grained sandstone to siltstone
39R-1, 69-71	h	8	278.69	2.44	2.79	2.33	19.49	3.99	Laminated fine-grained sandstone
41R-1, 29-31	h	6	297.59	1.86	2.69 (2.69)	3.69	31.10 (31.10)	2.95	Fine-grained sandstone with clay-rich matrix, small amounts of quartz, silt, and sulfide
42R-1, 101-103	h	14	307.91	2.27	2.81	3.17	29.60	3.00	Laminated siltstone
43R-1, 31-33	h	4B	316.81	2.31	2.79	3.26	26.56	3.17	Sandstone
44R-1, 92-94	h	9	327.12	2.00	2.74 (2.74)	3.11	26.90 (26.90)	3.03	Laminated fine-grained sandstone; silt-rich matrix; no sulfides
46R-1, 34-36	h	6	345.84	2.37	2.80	2.74	23.90	2.99	Laminated fine-grained silty sandstone
47R-2, 28-30	h	4	356.88	2.32	2.81	3.07	26.49	3.28	Fine-grained sandstone
49R-1, 76-78	h	10	374.96	2.48	2.83	2.33	19.30	3.36	Laminated mudstone
51R-1, 100-102	h	14	394.40	2.57	2.82	1.58	13.57	NA	Siltstone with mudstone laminations
55R-1, 28-30	h	5A	431.98	2.75	2.86	0.85	6.07	3.91	Altered diabase; plagioclase altered to clay
59R-1, 83-85	h	12	461.53	2.58	2.99	2.72	20.40	3.05	Moderately phyric and pervasively altered basalt
60R-2, 26-28	h	3	465.96	2.86	2.96	0.67	4.82	2.48	Pervasively altered diabase with minor disseminated sulfides
65R-2, 71-73	h	9A	496.41	2.86	2.96 (2.97)	0.70	4.98 (4.50)	2.42	Highly altered basalt with mottled texture
169-1035F-									
4R-1, 79-81	h	8	32.89	4.19	4.75	1.89	14.78	7.18	Massive sulfide; mostly pyrite with smaller amounts of sphalerite
5R-2, 138-140	h	23	44.52	4.32	4.81	1.61	12.75	10.95	Massive sulfide; mostly pyrite/marcasite with smaller amounts of sphalerite
6R-1, 109-113	v	20	52.49	4.00	4.75	3.60	19.92	7.75	Massive sulfide; pore spaces seem to be interconnected
10R-1, 25-27	h		90.15	2.21	2.84 (2.78)	4.43	33.92 (30.60)	3.57	Sulfide-banded sediment; clay-rich matrix; disseminated sulfides
11R-1, 6-13	v		99.76	2.69	2.85 (2.83)	2.02	8.41 (8.90)	4.92	Sulfide-veined sediment; veins perpendicular to minicore axis; less sulfide than in Sample 169-856H-31R-1, 74–79 cm (h)
12R-1, 132-134	h	14	110.62	2.42	2.88 (2.63)	3.06	24.32 (16.60)	3.57	Sulfide-veined sediment hydrothermally altered to clay minerals; disseminated sulfides and one sulfide vein
13R-1, 42-44	h	1	119.42	2.06	2.89	5.89	43.87	2.64	Silty claystone with disseminated chalcopyrite and pyrrhotite
13R-2, 6-8	h	1	120.56	2.66	2.87 (2.85)	1.42	10.91 (11.70)	4.67	Medium-grained moderately indurated and hydrothermally altered sandstone; electrical short from sulfide veins
17R-1, 29-31	h	5	157.79	2.11	2.87 (2.98)	5.49	40.20 (45.80)	2.53	Laminated turbiditic sandstone with clay-rich matrix; no sulfides; deformed more than any other core
19R-1, 76-78	h	13	177.56	2.30	2.85	3.88	29.40	3.23	Medium-grained sandstone with siltstone laminations
169-1035H-									
2R-2, 77-79	h	3	11.07	3.52	4.36	3.14	25.11	3.42	Sulfide breccia with sulfide clasts
4R-1, 147-150	h		27.87	2.27	2.89	4.13	32.35	2.89	Sandstone with sulfide veins and disseminations
6R-1, 62-64	h		46.22	2.10	2.81	5.31	38.93	2.84	Siltstone with very minor disseminated sulfides

Table T1 (continued).

Core, section, interval, cm)	Orientation[1]	Piece number	Depth[2] (mbsf)	Bulk density (g/cm^3)	Grain density[3] (g/cm^3)	Pore-water volume (cm^3)	Porosity[3] (%)	Thermal conductivity[4] (W/[m·K])	Lithology and comments
8R-1, 17-20	h	3	65.07	2.21	2.81	4.20	33.29	2.85	Fine-grained sandstone with very fine laminations
14R-1, 27-29	h	5	123.27	2.47	2.85	2.69	20.20	3.95	Laminated siltstone with small sulfide veins
16R-3, 8-10	h	1	135.55	3.95	4.35	1.47	11.85	7.33	Massive sulfide and oxide sample
17R-3, 6-8	h	2	145.36	2.47	3.86	5.92	48.31	NA	Massive sulfide with brown sphalerite; chlorite-rich matrix
17R-4, 84-89	v	12	147.64	3.96	4.44	2.36	13.93	6.45	
20R-1, 77-80	h	17	171.87	2.61	2.94	2.11	16.95	3.57	Sulfide-veined silty sandstone
22R-1, 84-87	h	16	191.14	2.16	2.70	4.26	31.66	2.69	Laminated silty sandstone
23R-1, 110-113	h	18	201.00	2.17	2.81	4.35	35.16	2.82	Siltstone
24R-1, 6-9	h	1	209.56	2.28	2.86	3.99	30.69	2.93	Laminated fine-grained sandstone
25R-1, 120-123	h	19	220.30	2.26	2.91	4.60	33.86	3.25	Siltstone
26R-1, 23-26	h	4	228.93	2.38	2.86	3.32	25.70	3.66	Laminated silty claystone
27R-1, 74-77	h	11	239.04	2.43	2.82	2.79	21.52	3.65	Laminated fine-grained sandstone
27R-2, 26-29	h	3	239.98	2.50	2.82	2.18	17.28	4.09	Laminated fine-grained sandstone
169-1038I-									
43X-3, 58-61	h	8	404.98	2.87	2.92	0.34	2.60	NA	Fine-grained plagioclase-phyric basalt; vesicles filled with calcite; some sulfides present in groundmass
158-957C-									
7N-3, 15-17	h	3	22.50	2.79	2.98	NA	9.62	4.42	Anhydrite vein
11N-2, 32-34	h	1E	32.43	NA	NA	NA	NA	11.06	Pyrite-silica-anhydrite breccia
16N-2, 7-9	h	1B	47.77	3.90	3.99	NA	3.07	12.59	Silicified wallrock breccia
158-957G-									
3N-1, 12-14	h	2A	21.12	4.10	4.40	NA	9.14	12.68	Massive pyrite-anhydrite breccia
158-957H-									
5N-1, 4-6	h	1	26.74	4.62	4.96	NA	8.58	24.96	Massive granular pyrite
5N-2, 29-31	h	1D	27.89	4.33	4.69	NA	9.92	20.41	Silicified wallrock breccia
158-957O-									
2R-1, 34-36	h	7	8.28	3.94	4.27	NA	10.22	12.30	Nodular pyrite breccia
158-957P-									
6R-1, 11-13	h	3	26.61	4.23	4.56	NA	9.29	14.13	Nodular pyrite breccia
12R-2, 67-69	h	12	56.57	4.31	4.43	NA	3.42	21.10	Pyrite-silica breccia with silicified basalt clasts

Notes: All Leg 169 samples are from the Bent Hill area of Middle Valley except Sample 169-1038I-43X-3, 58–61 cm, (h), which is a basalt from the Escanaba Trough (see Fouquet, Zierenberg, Miller, et al., 1998, for exact hole locations). All Leg 158 samples are from Trans-Atlantic Geotraverse (TAG) (see Humphris, Herzig, Miller, et al., 1996, for exact hole locations). [1]Sample orientation: h = horizontal; v = vertical. [2]Approximate sample depths in meters below seafloor (mbsf) based on curated core depths. [3]Measurements in parentheses were performed at New England Research Laboratory. The rest of the measurements were performed at Rosenstiel School of Marine and Atmospheric Sciences (see "Appendix," p. 15). [4]Measurements performed at Pacific Geoscience Centre (see "Appendix," p. 15). NA = not available.

Table T2. Formation factor, resistivity, and permeability measurements as a function of confining pressure for samples from Middle Valley. (See table notes. Continued on next three pages.)

Core, section, interval (cm)	Orientation	Sample number	Depth (mbsf)	Lithology	Confining Pressure (MPa)	Formation factor (at 20 mHz)	Formation factor (at 1 kHz)	Formation factor (at 100 kHz)	Resistivity (Ωm)	Fluid conductivity (mS/cm)	Permeability (μD)	Permeability (m^2)
169-856H-												
20R-1, 22-24	h	1	103.82	Sulfide-veined siltstone						10.35		
					10	NA	NA	NA	NA		42.11	4.21E–17
					10	NA	NA	NA	NA		33.90	3.39E–17
					10	NA	NA	NA	NA		43.45	4.34E–17
					10	NA	NA	NA	NA		29.83	2.98E–17
					10	NA	NA	NA	NA		31.19	3.12E–17
					10	NA	NA	NA	NA		32.77	3.28E–17
					10	22.00	3.53	1.13	3.62		32.92	3.29E–17
					20	NA	3.76	NA	3.84		36.42	3.64E–17
					35	NA	3.58	NA	3.62		35.15	3.51E–17
					50	NA	3.67	NA	3.70		31.22	3.12E–17
					35	NA	4.07	NA	4.16		32.43	3.24E–17
					20	NA	3.90	NA	4.02		32.92	3.29E–17
					10	NA	3.57	NA	3.69		31.68	3.17E–17
					10	NA	NA	NA	NA		31.43	3.14E–17
21R-1, 78-80	h	2	114.18	Sulfide (with minor amounts of silt)						9.94		
					10	NA	NA	NA	NA		0.91	9.09E–19
					10	5.32	0.45	0.116	0.49		0.81	8.11E–19
					10	NA	0.43	NA	0.46		0.80	7.99E–19
					10	NA	0.42	NA	0.45		0.81	8.11E–19
					20	NA	0.46	NA	0.49		0.85	8.50E–19
					35	NA	0.39	NA	0.41		0.81	8.07E–19
					50	NA	0.21	NA	0.22		0.77	7.70E–19
					35	NA	0.39	NA	0.42		NA	NA
					20	NA	0.44	NA	0.48		NA	NA
					10	NA	0.39	NA	0.43		0.95	9.51E–19
					10	NA	0.41	NA	0.45		0.76	7.58E–19
22R-2, 65-67	h	3	119.25	Sulfide-veined siltstone						10.00		
					10	NA	0.007	NA	0.007		4.29	4.29E–18
					15	NA	NA	NA	NA		4.49	4.49E–18
					25	NA	NA	NA	NA		4.49	4.49E–18
					35	NA	NA	NA	NA		4.72	4.72E–18
					50	NA	NA	NA	NA		4.72	4.72E–18
					35	NA	NA	NA	NA		4.72	4.72E–18
					25	NA	NA	NA	NA		4.72	4.72E–18
					15	NA	NA	NA	NA		4.72	4.72E–18
					10	NA	NA	NA	NA		4.49	4.49E–18
22R-2, 124-130	v	4	119.84	Sulfide-veined siltstone						10.00		
					10	NA	0.006	NA	0.006		0.23	2.32E–19
					15	NA	NA	NA	NA		0.12	1.20E–19
					25	NA	NA	NA	NA		0.06	6.45E–20
					35	NA	NA	NA	NA		0.04	3.53E–20
					50	NA	NA	NA	NA		0.02	2.45E–20
25R-3, 16-18	h	5	147.96	Siltstone-claystone with disseminated sulfides						8.22		

Table T2 (continued).

Core, section, interval (cm)	Orientation	Sample number	Depth (mbsf)	Lithology	Confining Pressure (MPa)	Formation factor (at 20 mHz)	Formation factor (at 1 kHz)	Formation factor (at 100 kHz)	Resistivity (Ωm)	Fluid conductivity (mS/cm)	Permeability (μD)	Permeability (m^2)
					10	23.30	21.70	20.70	29.40		3.87	3.87E–18
					15	NA	NA	NA	NA		3.69	3.69E–18
					25	NA	NA	NA	NA		3.63	3.63E–18
					35	NA	NA	NA	NA		3.62	3.62E–18
					50	NA	23.40	NA	30.70		NA	NA
					50	NA	23.50	NA	30.70		3.27	3.27E–18
					35	NA	NA	NA	NA		3.70	3.70E–18
					25	NA	NA	NA	NA		3.79	3.79E–18
					15	NA	NA	NA	NA		3.85	3.85E–18
					10	NA	NA	NA	NA		3.96	3.96E–18
31R-1, 9-11	h	6	201.09	Sulfide-banded sandstone						10.01		
					10	NA	0.053	NA	0.056		130.75	1.31E–16
					10	NA	0.058	NA	0.061		64.86	6.49E–17
					10	NA	0.058	NA	0.062		65.92	6.59E–17
					15	NA	NA	NA	NA		72.60	7.26E–17
					25	NA	NA	NA	NA		69.28	6.93E–17
					35	NA	NA	NA	NA		60.93	6.09E–17
					50	NA	NA	NA	NA		50.90	5.09E–17
					35	NA	NA	NA	NA		49.18	4.92E–17
					25	NA	NA	NA	NA		52.30	5.23E–17
					15	NA	NA	NA	NA		56.52	5.65E–17
					10	NA	NA	NA	NA		96.04	9.60E–17
					10	NA	NA	NA	NA		50.57	5.06E–17
					10	NA	NA	NA	NA		50.21	5.02E–17
31R-1, 74-79	v	7	201.74	Sulfide-banded sandstone						10.01		
					10	4.27	2.69	2.37	3.35		1.39	1.39E–18
					10	NA	3.07	NA	NA		1.33	1.33E–18
					15	NA	NA	NA	NA		1.02	1.02E–18
					25	NA	NA	NA	NA		1.07	1.07E–18
					35	NA	NA	NA	NA		1.07	1.07E–18
					50	NA	3.72	NA	4.00		0.66	6.60E–19
					35	NA	NA	NA	NA		1.16	1.16E–18
					25	NA	NA	NA	NA		1.08	1.08E–18
					15	NA	NA	NA	NA		0.95	9.50E–19
					10	NA	NA	NA	NA		0.93	9.30E–19
41R-1, 29-31	h	8	297.59	Fine-grained sandstone						10.09		
					10	NA	NA	NA	NA		157.54	1.58E–16
					10	NA	NA	NA	NA		158.58	1.59E–16
					10	8.89	8.87	9.02	9.63		158.10	1.58E–16
					20	NA	9.17	NA	9.87		175.77	1.76E–16
					35	NA	9.45	NA	10.10		157.39	1.57E–16
					50	NA	9.88	NA	10.50		155.28	1.55E–16
					35	NA	9.73	NA	10.50		91.81	9.18E–17
					20	NA	9.51	NA	10.30		95.39	9.54E–17
					10	NA	8.85	-	9.63		87.95	8.80E–17
44R-1, 92-94	h	9	327.12	Fine-grained sandstone						9.94		
					10	14.10	14.00	14.30	15.10		52.66	5.27E–17
					10	NA	14.10	NA	15.20		67.87	6.79E–17

Table T2 (continued).

Core, section, interval (cm)	Orientation	Sample number	Depth (mbsf)	Lithology	Confining Pressure (MPa)	Formation factor (at 20 mHz)	Formation factor (at 1 kHz)	Formation factor (at 100 kHz)	Resistivity (Ωm)	Fluid conductivity (mS/cm)	Permeability (μD)	Permeability (m^2)
					10	NA	14.10	NA	15.20		52.19	5.22E–17
					20	NA	14.60	NA	15.60		57.42	5.74E–17
					35	NA	14.80	NA	15.80		58.70	5.87E–17
					50	NA	14.80	NA	15.70		51.80	5.18E–17
					35	NA	14.60	NA	15.80		52.73	5.27E–17
					20	NA	14.30	NA	15.50		52.75	5.27E–17
					10	NA	13.60	NA	14.80		50.90	5.09E–17
					10	NA	13.70	NA	14.90		NA	NA
65R-2, 71-73	h	10	496.41	Altered basalt						9.82		
					10	372	324	294	354		0.04	3.70E–20
					20	NA	346	NA	376		NA	NA
					35	NA	386	NA	417		NA	NA
					50	NA	432	NA	466		NA	NA
					35	NA	416	NA	455		NA	NA
					20	NA	387	NA	424		NA	NA
					10	NA	352	NA	386		NA	NA
					10	NA	357	NA	389		NA	NA
					10	NA	356	NA	388		NA	NA
169-1035F-												
10R-1, 25-27	h	11	90.15	Sulfide-banded claystone						10.29		
					10	12.90	5.38	4.05	5.70		1.33	1.33E–18
					10	NA	5.28	NA	5.64		1.82	1.82E–18
					10	NA	5.26	NA	5.60		NA	NA
					10	NA	5.27	NA	5.62		2.02	2.02E–18
					20	NA	4.44	NA	4.68		1.62	1.62E–18
					35	NA	3.45	NA	3.61		1.00	1.00E–18
					50	NA	3.10	NA	3.25		0.56	5.58E–19
					35	NA	NA	NA	NA		0.59	5.94E–19
					20	NA	NA	NA	NA		0.66	6.55E–19
					10	NA	4.73	NA	5.01		0.68	6.83E–19
11R-1, 6-13	v	12	99.76	Sulfide-veined siltstone-claystone						11.00		
					10	30.50	10.50	7.86	10.50		0.05	4.50E–20
					10	NA	9.08	NA	8.99		NA	NA
					10	NA	9.06	NA	8.97		NA	NA
					10	NA	9.75	NA	9.65		NA	NA
					10	NA	9.37	NA	9.28		NA	NA
					10	NA	9.90	NA	9.80		NA	NA
					20	NA	10.20	NA	9.99		NA	NA
					35	NA	10.80	NA	10.60		NA	NA
					50	NA	11.40	NA	11.10		NA	NA
					35	NA	11.50	NA	11.30		NA	NA
					20	NA	11.30	NA	11.20		NA	NA
					10	NA	11.00	NA	11.00		NA	NA
					10	NA	10.80	NA	10.80		NA	NA
12R-1, 132-134	h	13	110.62	Sulfide-veined siltstone						10.35		
					10	NA	NA	NA	NA		10.98	1.10E–17
					10	13.40	6.14	4.88	6.28		9.96	9.96E–18
					10	NA	5.93	NA	6.10		10.31	1.03E–17

Table T2 (continued).

Core, section, interval (cm)	Orientation	Sample number	Depth (mbsf)	Lithology	Confining Pressure (MPa)	Formation factor (at 20 mHz)	Formation factor (at 1 kHz)	Formation factor (at 100 kHz)	Resistivity (Ωm)	Fluid conductivity (mS/cm)	Permeability (μD)	Permeability (m^2)
					20	NA	5.39	NA	5.54		10.86	1.09E–17
					35	NA	5.87	NA	6.00		9.75	9.75E–18
					50	NA	6.33	NA	6.46		8.32	8.32E–18
					35	NA	6.32	NA	6.54		8.54	8.54E–18
					20	NA	6.09	NA	6.34		8.65	8.65E–18
					10	NA	5.52	NA	5.77		8.49	8.49E–18
					10	NA	5.46	NA	5.68		8.66	8.66E–18
					10	NA	5.40	NA	5.62		NA	NA
					10	NA	5.64	NA	5.86		NA	NA
13R-2, 6-8	h	14	120.56	Medium-grained sandstone						11.32		
					10	NA	NA	NA	NA		6.96	6.96E–18
					10	NA	NA	NA	NA		7.03	7.03E–18
					10	24.00	4.04	1.19	3.85		7.03	7.03E–18
					10	NA	3.98	NA	3.79		7.25	7.25E–18
					20	NA	4.14	NA	3.91		6.16	6.16E–18
					35	NA	4.49	NA	4.24		5.10	5.10E–18
					50	NA	5.03	NA	4.70		4.71	4.71E–18
					35	NA	5.61	NA	5.34		4.65	4.65E–18
					20	NA	5.13	NA	4.93		4.70	4.70E–18
					10	NA	4.33	NA	4.16		4.54	4.54E–18
					10	NA	3.39	NA	3.23		4.45	4.45E–18
					10	NA	3.27	NA	3.11		4.46	4.46E–18
					10	NA	NA	NA	NA		4.61	4.61E–18
					10	NA	NA	NA	NA		4.59	4.59E–18
17R-1, 29-31	h	15	157.79	Laminated sandstone						11.80		
					10	8.55	7.79	7.63	7.15		14.27	1.43E–17
					10	NA	7.83	NA	7.18		12.01	1.20E–17
					10	NA	7.78	NA	7.20		12.48	1.25E–17
					20	NA	8.03	NA	7.37		12.79	1.28E–17
					35	NA	8.22	NA	7.47		NA	NA
					50	NA	11.70	NA	10.60		1.73	1.73E–18
					35	NA	11.30	NA	10.40		1.81	1.81E–18
					20	NA	10.50	NA	9.65		2.15	2.15E–18
					10	NA	9.20	NA	8.44		2.39	2.39E–18
					10	NA	9.21	NA	8.37		3.23	3.23E–18
					10	NA	NA	NA	NA		3.62	3.62E–18

Notes: Three samples with electrical shorts have resistivities reported at 1 kHz using method 1 (see "Appendix," p. 15). The sample orientation with respect to the borehole is denoted by either an h (horizontally oriented sample) or v (vertical orientation). Fluid conductivities measured at the beginning of each experiment are also included. Sample numbers represent numbers used in Figures 3 through 10, and 15. NA = not available.

Table T3. Comparison of thermal conductivity measurements from Middle Valley and Trans-Atlantic Geotraverse. (**See table notes.** Continued on next page.)

Core, section	Interval (cm) Top	Interval (cm) Bottom	Depth (mbsf)	Piece number	Reference	Divided bar (W/[m·K])	Half space (W/[m·K])
Measurements of the same sample							
169-856H-							
20R-1	22	24	103.82	3A	1a	3.98	NA
20R-1	15	24	103.75	3A	2	NA	4.05
29R-1	55	57	182.25	9	1a	3.45	NA
29R-1	50	60	182.20	9	2	NA	3.20
32R-1	53	55	211.13	9A	1a	5.10	NA
32R-1	45	55	211.05	9A	2	NA	5.05
41R-1	29	31	297.59	6	1a	2.95	NA
41R-1	26	34	297.56	6	2	NA	2.80
42R-1	101	103	307.91	14	1a	3.00	NA
42R-1	99	105	307.89	14	2	NA	2.90
43R-1	31	33	316.81	4B	1a	3.17	NA
43R-1	26	35	316.76	4B	2	NA	3.25
44R-1	92	94	327.12	9	1a	3.03	NA
44R-1	90	97	327.10	9	2	NA	3.35
46R-1	34	36	345.84	6	1a	2.99	NA
46R-1	32	42	345.82	6	2	NA	3.10
47R-2	28	30	356.88	4	1a	3.28	NA
47R-2	26	33	356.86	4	2	NA	3.25
49R-1	76	78	374.96	10	1a	3.36	NA
49R-1	73	81	374.93	10	2	NA	4.30
55R-1	28	30	431.98	5A	1a	3.91	NA
55R-1	27	34	431.97	5A	2	NA	4.00
65R-2	71	73	496.29	9A	1a	2.42	NA
65R-2	65	73	496.23	9A	2	NA	2.35
169-1035F-							
5R-2	138	140	44.52	23	1a	10.95	NA
5R-2	138	140	44.52	23	1b	11.60	NA
5R-2	138	140	44.52	23	1c	11.73	NA
5R-2	138	148	44.52	23	2	NA	9.75
6R-1	109	113	52.49	20	1a	7.75	NA
6R-1	109	113	52.49	20	1b	7.80	NA
6R-1	109	113	52.49	20	1c	7.01	NA
17R-1	29	31	157.79	5	1	2.53	NA
17R-11	25	33	157.75	5	2	NA	2.25
169-1035H-							
16R-3	8	10	135.55	1	1a	7.33	NA
16R-3	1	17	135.48	1	2	NA	8.55
27R-3	26	29	239.98	3	1a	4.09	NA
27R-3	22	35	239.94	3	2	NA	4.07
158-957C-							
7N-3	15	17	22.50	3	1a	4.42	NA
7N-3	10	25	22.45	3	4	NA	5.37
11N-2	32	34	32.43	1E	1a	11.06	NA
11N-2	28	36	32.39	1E	4	NA	8.68
14N-1	13	15	40.33	2	3	13.00	
14N-1	18	20	40.38	2	3	13.50	NA
14N-1	10	22	40.30	2	4	NA	8.34
158-957F-							
1N-1	55	57	1.55	10B	3	5.02	NA
1N-1	52	64	1.52	10B	4	NA	6.10
158-957H-							
5N-1	4	6	26.74	1	1a	24.95	NA
5N-1	4	6	26.74	1	1b	23.90	NA

Table T3 (continued).

Core, section	Interval (cm) Top	Bottom	Depth (mbsf)	Piece number	Reference	Divided bar (W/[m·K])	Half space (W/[m·K])
5N-1	4	6	26.74	1	1c	26.08	NA
5N-1	33	35	27.03	5A	3	14.00	NA
5N-1	29	40	26.99	5A	4	NA	10.28
5N-2	29	31	27.89	1D	1a	20.41	NA
5N-2	27	33	27.87	1D	4	NA	8.29
158-957G-							
3N-1	12	14	21.12	2A	1a	12.68	NA
3N-1	15	17	21.15	2A	3	14.24	NA
3N-1	6	20	21.06	2A	4	NA	8.59
158-957O-							
2R-1	34	36	8.28	7	1a	12.30	NA
2R-1	37	39	8.27	7	3	14.62	
2R-1	30	40	8.24	7	4	NA	10.48
158-957P-							
12R-2	67	69	56.57	12	1a	21.10	NA
12R-2	67	69	56.57	12	1b	19.80	NA
12R-2	67	69	56.57	12	1c	20.65	NA
139-856H-							
3R-1	16	18	22.26	3A?	5	7.30	NA
3R-1	28	34	22.38	3A?	6	NA	3.77
9R-1	59	61	53.13	8	5	12.10	NA
9R-1	56	65	53.10	8	6	NA	6.29
13R-1	40	42	71.30	5	5	6.50	NA
13R-1	30	42	71.20	5	6	NA	4.64
Close but not the same piece							
158-957C-							
11N-2	18	20	32.29	1C	3	13.58	NA
11N-2	28	36	32.39	1E	4	NA	8.68
11N-2	22	24	32.32	1D	3	14.95	NA
11N-2	28	36	32.39	1E	4	NA	8.68
11N-2	40	42	32.51	1F	3	8.77	NA
11N-2	28	36	32.39	1E	4	NA	8.68
Discrepancy on the interval between samples (listed as same but intervals do not match)							
139-856H-							
3R-3	107	109	25.80	11?	5	5.10	NA
3R-3	91	98	25.62	10?	6	NA	4.05
Listed as within 10 cm but measurements were performed in different pieces and could be meters apart							
158-957C-							
16N-1	8	10	46.28	2	3	10.80	NA
16N-1	14	22	46.34	3	4	NA	5.73
158-957O-							
4R-1	40	42	16.30	8	3	13.81	NA
4R-1	23	34	16.19	6	4	NA	10.15

Notes: The numbers in the Reference column correspond to the following data sets: 1a = New data, measurements made at Pacific Geoscience Centre; 1b = measurements made at University of Utah; 1c = measurements made at Prague. 2 = Leg 169, Fouquet, Zierenberg, Miller, et al., 1998. 3 = Rona et al., 1998. 4 = Leg 158, Humphris, Herzig, Miller, et al., 1996. 5 = Gröschel-Becker et al., 1994. 6 = Leg 139, Davis, Mottl, Fisher, et al., 1992. Piece number (?) = uncertainty on the previously reported numbers. NA = not available.

Table T4. Formation factor and resistivity measurements as a function of sample and fluid conductivity.

Core, section, interval (cm)	Orientation	Formation factor	Fluid conductivity (mS/cm)	Resistivity (Ωm)	Sample conductivity (mS/cm)
169-865H-					
25R-3, 16-18	h	20.1	5.31	37.8	28.5
		25.5	10.9	23.4	46.2
		22.4	8.88	25.2	42.3
		22.2	8.85	25.1	42.7
		25.3	13	17.8	56.2
		24.2	16	15.5	71.5
		22.4	7.56	29.4	36.7

Note: h = horizontal sample orientation.